

1 A new Morphology-based classification scheme
2 characterization for of intermediate to silicic lava flows:
3 application to the Central Andean Volcanic Zone

4 Jose Pablo Sepulveda ^{a,b*}, Raffaello Cioni ^a, Alvaro Aravena ^{c,d}

5 ^a Dipartimento di Scienze della Terra, Università degli studi di Firenze, Via Giorgio la Pira, 4, 50121
6 Florence, Italy

7 ^b Millennium Institute on Volcanic Risk Research - Ckelar Volcanoes ~~Ckelar Volcanoes~~, Universidad
8 Católica del Norte, Avenida Angamos 0610, Antofagasta, Chile

9 ^c Laboratoire Magmas et Volcans, Université Clermont Auvergne, CNRS, IRD, OPGC, Clermont-
10 Ferrand, France

11 ^d Facultad de Ciencias Básicas, Universidad Católica del Maule, Talca, Chile

12

13 * Corresponding author. E-mail address: josepablo.sepulvedabirke@unifi.it

14 Highlights:

- 15 - Morphology-based characterization allows us to distinguish different types of
16 intermediated lava flows
- 17 - The different morphologies result from the combined effect of the progressively
18 changing lava flow rheology, effusion rate, and topography
- 19 - A S-transform spectral analysis of lava flows grayscale satellite image can be used to
20 extract the dominant wavelengths of surface folding

21 **Abstract**

22 The morphology of a lava flow records the eruptive dynamics that governed its emplacement,
23 evolution, and the rheological properties of the erupted magma. Although the dynamics and
24 morphological classification of mafic lava flows have been widely addressed, the
25 characterization of the morphological features of intermediate to silicic lavas is still not
26 exhaustive. In this study, we perform a morphological-based characterization of lava flows
27 based on DEM-derived data and satellite images. We analyzed a dataset of 49 intermediate
28 to silicic lava flows from the Central Andean Volcanic Zone and quantified the maximum
29 wavelength of their surface ridges, described as folds, and their relationship with thickness

30 distribution, pre-surface slope, composition, and rheology. Furthermore, we introduced a
31 Fourier analysis to quantitatively characterize the lava flows' plain-view shape and a novel
32 method based on an S-Transform spectral analysis of grayscale satellite images to assess the
33 surface folding pattern. We distinguish 4 main types of lava flows in the andesite to dacite
34 compositional range. *Ridged lavas* have highly arcuate ridges with convex surfaces, large
35 thickness, and a curved, smooth frontal lobe. *Coulee lavas* have intermediate characteristics
36 between lava flows and domes, with relatively simple shapes, lengths that do not significantly
37 exceed their width, vents generally located in the central zone of the flow, prominent ridges
38 and crumble breccias. *Leveed lavas*, which include a wide range of flow lengths, have the
39 simplest shapes, exhibiting marked channelization and a unique frontal toe of maximum
40 thickness. *Breakout lavas* have the most complex plain-view shapes, with lateral and frontal
41 lobes, poorly developed levees, and wider and thicker fronts. *Transitional lavas*, with
42 intermediate characteristics in terms of folding patterns and shapes, are also recognized. We
43 show that the maximum wavelength of surface deformation is not continuous along the flow
44 surface and spatially correlates with thickness distribution. In addition, the maximum
45 wavelength is poorly correlated with SiO₂ content and weakly correlated with lava viscosity,
46 showing a positive correlation with the gravitational component of the shear stress applied to
47 the flow. Results suggest that the pre-eruptive slope and viscosity, along with the effusion
48 rate, play a primary role in governing the general dynamics of the flow and thus the resulting
49 lava morphology, impacting different measurable features such as length, width, branching,
50 and general deformation dynamics of the flow. The recognition of the main characteristics
51 of the different lava types and their controlling factors represents a first step for interpreting
52 lava flow morphology in terms of the eruption characteristics. This strategy can be adopted
53 for analyzing and interpreting remotely terrestrial and extra-terrestrial lava flows.

54 Keywords: Lava flow morphology, Dacite, Andes, blocky lava, folds

55 1. Introduction

56 Lava flows are the most common eruptive products on Earth and extra-terrestrial surfaces.
57 They exhibit a wide variation spectrum in terms of composition, size, shape, and surface and
58 internal structures, varying from thin flows with relatively smooth surfaces to voluminous
59 lava flows hundreds of meters thick (Kilburn, 2000; Harris and Rowland, 2015). The

60 morphological characteristics of lava flows are a consequence of the combined effect of
61 eruption source parameters (e.g., effusion rate and source geometry), magma properties (e.g.,
62 rheology, controlled by composition, temperature, and crystal content), and the
63 characteristics of the terrain over which the lavas flowed (Hulme, 1974; Griffiths et al., 2003;
64 Lescinsky et al., 2007). Thus, the morphology of a given lava flow can provide insights into
65 the erupted magma properties and emplacement processes (Griffiths and Fink, 1992; Chevrel
66 et al., 2013; Tolometti et al., 2020), allowing us to understand the fundamental parameters
67 and dynamics that controlled the eruption.

68 In order to characterize the surface of lava flows, a frequently adopted strategy is based on a
69 descriptive tripartite classification, including pahoehoe, a'ā, and blocky lavas (Macdonald,
70 1953). Several studies have focused on active pahoehoe and a'ā lava flows (e.g., at Hawaii,
71 Mt. Etna, Iceland, among other case studies) and on analog laboratory experiments to
72 simulate basaltic flows (Hallworth et al., 1987; Fink and Griffiths, 1990; Griffiths and Fink;
73 1992a, 1992b; Gregg and Fink, 1995, 1996, 2000; Kerr et al., 2006). Thanks to them, the
74 emplacement dynamics of mafic flows are reasonably well-understood, and a robust
75 morphological classification has been developed (Wentworth and Macdonald, 1953;
76 Macdonald, 1967; Fink and Fletcher, 1978; Kilburn, 1990; Harris et al., 2016, and references
77 therein). Regarding highly evolved lavas, increasing attention has been paid during the last
78 decades (Fink, 1980, 1983; de Silva et al., 1994; Castro and Cashman, 1999; Castro et al.,
79 2002; Harris et al., 2002; Pyle and Elliot, 2006; Lescinsky et al., 2007; Tuffen et al., 2013;
80 Castro et al., 2013; Farquharson et al., 2015; Magnall et al., 2017, 2018; Bullock et al., 2018;
81 Deardorff et al., 2019; Legget et al., 2020; Andrews et al., 2020). Most of these studies have
82 been focused on rhyolitic and/or obsidian-like flows, while, even though a suite of
83 investigations on specific case studies is available in the literature (Borgia and Linneman,
84 1990; Naranjo et al., 1992; de Silva et al., 1994; Watts et al., 2002; Harris et al., 2002; Cioni
85 and Funedda, 2005; Pyle and Elliot, 2006; Vallance et al., 2008; Latutrie et al., 2017; among
86 others), less attention has been paid to the analysis of the general laws controlling the
87 evolution and emplacement of lavas in the andesite-to-dacite compositional range.

88 In this study, we present a morphology-based characterization of andesitic to dacitic lavas
89 based on the analysis of easily accessed satellite imagery and topographic data, considering

90 **their**-plain-view **shape, thickness and characteristics of the upper surface**. In particular, we
91 analyse the surface texture in terms of folding patterns and maximum wavelength, and we
92 also evaluate their relationship with thickness distribution, pre-surface slope, composition,
93 and rheology. In addition, we introduce a Fourier Descriptors analysis for quantifying the
94 plain-view shape of the lava flows and a novel method based on a S-transform spectral
95 analysis of grayscale satellite image data to describe the surface folding pattern
96 quantitatively. On the basis of our remote characterization, we define 4 main categories for
97 intermediate to silicic lava flows. We conclude that the investigated lava flows cannot be
98 distinguished only based on few simple, univocal characteristics (like for example the
99 pahoehoe or a'ā surface of basaltic lavas) but by a sum of multiple observations. Although
100 this fact does not allow to build a real "classification scheme" (where classification is
101 intended as "a systematic arrangement in groups or categories according to established
102 criteria; Merriam Webster Dictionary, 2002" and in which each group is strictly defined by
103 a list of univocal criteria), the recognition and characterization of some morphological
104 features can inform about the main processes controlling the emplacement and final
105 morphology of these lava flows.

106 **2. Background on lava flow morphology-based classification**

107 **2.1 Blocky lavas and folding**

108 In the study of intermediate to silica-rich lavas, which are frequently characterized by the
109 accumulation of angular blocks formed by the breakage of the rigid upper lava surface, a
110 commonly adopted descriptive term is blocky-lava (**Finch, 1933**). This general term is used
111 for both obsidian-like and crystal-rich flows, with variable features of banding, shear
112 patterns, foliation, folding, and eventual blocky and/or rubbly breccias (Macdonald 1972;
113 Fink, 1980; Cas and Wright, 1987; Kilburn, 1990; 2000; Anderson and Fink, 1992; Cioni
114 and Funedda, 2005; Harris et al., 2016; Leggett et al., 2020). However, obsidian-like and
115 crystal-rich flows present different rheological and morphological features, and a wide
116 variety of deformation patterns are expected to operate during their emplacement (Table 1).

117 Silica-rich, obsidian-like flows are characterized by autobrecciated upper surfaces and by a
118 complex internal sequence that typically includes four lithofacies: lithoidal rhyolite (i.e.,
119 welded, generally devitrified), coarsely vesicular pumice, flow-banded obsidian, and fine

120 vesicular pumice (Fink, 1983; Manley and Fink 1987; Castro and Cashman, 1999, Bullock
121 et al., 2018, Table 1). Multiple generations and scales of ogives and crease structures occur
122 along with the upper surface of the flow. Although these ogives were first interpreted as
123 derived from the folding of the upper portion of the lava flow (Fink, 1980), other authors
124 suggest they suggested that they are fracture-bound structures rather than folds (Cas and
125 Wright, 1988; Andrews et al.; 2020). While obsidian lava flows remain the most studied
126 examples of silicic flows, Cioni and Funedda (2005) showed how deformation of crystal-
127 rich, lithoid silicic lava flows could develop different structures compared to glassy lavas,
128 with the formation of foliation surfaces that mainly control the lava movement. Formation of
129 different fold generations was clearly demonstrated in these lava flows (e.g. Figs. 8 and 9 in
130 Cioni and Funedda, 2005; Harris and Rowland, 2015), while nearly vertical fracture planes
131 (ramps) mainly develop in the frontal sectors of the lava flows where maximum strain
132 accumulated. Similarly, andesites and dacites are often pervasively foliated and fractured,
133 with basal and top breccias. Ridges occur on the flow surface as alternating arcuate peaks
134 and troughs with the concavity arranged perpendicular to the flow direction in the central
135 portions of the channel and subparallel to the flow direction along the outer margins (Fink,
136 1980; Cioni and Funedda, 2005).

137 By analogy with crystal-rich silicic lava flows, we interpret the ridge structures in andesites
138 and dacites as folds formed by compression. The relatively rigid, rapidly solidified crust
139 deforms with a brittle behavior forming the upper blocky surface, while the rest of the lava
140 body deforms plastically, inducing shear (Cioni and Funedda, 2005; Pyle and Elliot, 2006;
141 Lescinsky et al., 2007; Deardorff et al., 2019). At the base of these lavas, superimposed
142 penetrative foliations may govern folding (Cioni and Funedda, 2005). Shear planes
143 associated with these foliations are flow-parallel at the margins of the lava and sub-horizontal
144 to the flow base (Cioni and Funedda, 2005) and may act as sliding surfaces triggering folding
145 at different scales of the entire inner flow and surface ridges or as ramp structures, arranging
146 the movement and deformation of the flow through faulting during stick-slip processes (Cas
147 and Wright, 1988; Cioni and Funedda, 2005; Harris et al., 2016). Superimposed generations
148 of folds with progressively increasing wavelength and amplitude form when the tightly-
149 arranged, first-generation folds can no longer accommodate further flow-parallel shortening,
150 and compressional forces continue to act on the flow. The blocky surface of these lavas may

151 be rapidly removed by erosion, leaving uncovered the internal, deformed part of the flow
152 (Fink, 1980; Gregg et al., 1998; Cioni and Funedda, 2005; Farrel et al., 2018). Brittle
153 deformation dominates at the front of the lava flow or during the final phases of its
154 emplacement, forming crease structures and tensile fractures (Anderson and Fink, 1992;
155 Cioni and Funedda, 2005).

156

157 **Table 1.** Summary of the main characteristics for obsidian-like flows and crystalline andesites to
 158 dacites. FVP: fine vesicular pumice, CVP: coarse vesicular pumice. ^a Fink (1983), ^b Manley and Fink
 159 (1987), ^c Bullock et al. (2018), ^d Andrews et al. (2020), ^e Harris et al. (2016), ^f Cioni and Funedda
 160 (2005), ^g Cas and Wright (1987).

Lava type	Stratigraphy	Structures	Deformation mechanism
Obsidian like Rhyolitic	(i) basal breccia, (ii) thin layered obsidian with spherulites, (iii) devitrified to crystalline rhyolite, (iv) thick obsidian ranging from FVP lithofacies with small irregular-to-acicular vesicles to alternating centimeter-scale layers of obsidian with centimeter to meter-scale layers of CVP lithofacies, and (v) upper breccia ^{a, b, c}	Ogive Crease Autobreccia	Mainly brittle, disrupting and tilting of the surface ^{d, e}
Crystal rich andesites to dacites (rhyolites)	Basal auto-breccia with a massive core, sometimes well-developed flow foliation, columnar or blocky jointing, and a top breccia ranging from large subrounded rubbly clast to sub-angular obsidian and lithoid blocks ^{e, f, g}	Ridge Folds Ramps Crease Foliation Autobreccia	Synemplacement progressive folding due to compression. Thrust and ramp structures in the frontal sectors. ^f

161
162

163 2.2. Lava flow morphology from analog experiments

164 Analog experiments on lava flow morphology may help to classify the shape and
 165 morphological features of silicic lava flows, although many of these experiments were
 166 planned to simulate basaltic lavas. Hallworth et al. (1987) investigated the role of effusion
 167 rate, slope, and viscosity-temperature dependence in determining the morphology of basaltic
 168 lava flows. They qualitatively classified lava flows into (1) straight, open-channel flows,
 169 characterized by a single flow with a straight open channel bounded by levees; (2)
 170 meandering, temporarily roofed flows, which show overflow and breakout at their margins,
 171 and (3) compound flows, characterized by the establishment of tube systems. Later, Fink and
 172 Griffiths (1990) investigated the effect of a solidifying crust on the dynamics and surface
 173 morphology of radial viscous-gravity currents. They experimented with PEG wax, producing
 174 five distinct flow morphologies by systematically varying the cooling and effusion rates:
 175 pillows, rift, folded, levees, and no-crust flows. Griffiths and Fink (1992a) proposed that the
 176 ratio between the characteristic times of surface solidification and lateral flow advection is
 177 strictly related to the surface morphology. Many other studies from the same group furtherly
 178 refined these observations (Griffiths, 2000 and references therein).

179 The attempts to classify morphologically more evolved, high-viscosity lavas mainly focused
 180 on domes. Blake (1990) defined four types of domes: upheaved plugs, peleean, low lava, and

181 coulees. Afterward, Griffiths and Fink (1997) and Fink and Griffiths (1998) combined
182 experimental models with field measurements of active extrusions and remote sensing
183 observation of Holocene domes. They showed that the morphology of lava domes is related
184 to their eruption conditions and classified them into four main types; spiny, lobate, platy, and
185 axisymmetric domes. They also suggested that eruption conditions could be related through
186 a dimensionless parameter encompassing the eruption rate, magma rheology, and thickness
187 of the cooling surface. Finally, Lyman et al. (2004) performed laboratory experiments with
188 a PEG-kaolin slurry extruded into cold water, testing variable experimental conditions in the
189 slope, effusion rate, and water temperature. They distinguished four types of domes and
190 related lava flows morphologies: (1) spiny domes, with spine-like lobes similar to an up-
191 heaved plug; (2) lobate flows, characterized by smooth sides and wave-like ridges; (3) platy
192 flows, with a rough surface with small step-like ridges, and (4) no-crust flows, which
193 typically develop a crust only in their outermost margins. Transitions between the different
194 morphologies commonly occur. In addition, they calculated the yield strength or effusion rate
195 for lava domes based on their morphology, slope and ψ_B , suggesting the following equation:

196
$$\psi_B = (g\Delta\rho/\sigma_0)^3 Q t_s \quad (1)$$

197 where g is gravitational acceleration, $\Delta\rho$ is the density difference between magma and
198 environment, σ_0 is the yield strength, Q is the volumetric effusion rate and t_s is the
199 characteristic time for surface solidification.

200 **3. Methods**

201 The observation of structures on the scale of meters to hundreds of meters in andesitic to
202 dacitic lava flows clearly shows that a set of surface features may be introduced to
203 complement the classification schemes summarized above, particularly for leeved or folded
204 flows. For this reason, we present in this section a series of procedures to characterize
205 quantitatively the surface structures and morphology of a wide set of intermediate to silicic
206 lava flows.

207 **3.1 The lava flow dataset**

208 We selected a large set of examples from the Andes Central Volcanic Zone (CVZ) to address
209 the morphological characteristics of intermediate lava flows. The CVZ was selected due to
210 the relatively restricted compositional range that characterizes this volcanic arc (mainly
211 andesitic to dacitic magmas; Stern, 2004; Wörner et al., 2018). The hyper-arid climate
212 conditions since the Miocene (Dunai et al., 2005) caused the formation of unvegetated
213 surfaces and extremely-low erosion rates, so that a remarkable number of stratovolcanoes
214 and lava flows with well-preserved surface structures are present. This study includes 49
215 andesitic to dacitic lava flows emplaced during the Pleistocene (Table 2, Supplementary
216 material 1) selected from 27 volcanic systems, with compositions ranging from 58.7 to 68.3
217 wt% SiO₂. These lava flows account for a wide spectrum of morphological features, with
218 well-preserved ridges, creases, levees, and crumble breccia structures.

219 **3.2 Compiled information and lava flow characterization**

220 **3.2.1 Analysis of DEM-derived data**

221 We adopted a 12 m TanDEM-X (Krieger et al., 2007) for most of the studied lava flows and
222 an ALOS PALSAR DEM (12.5 m pixel resolution) for Tata Sabaya, Isluga, El Misti, and
223 Uturuncu volcanoes. Topographic data were used to extrapolate the pre-eruptive surface,
224 thickness, volume, and roughness for each lava flow.

225 Following Kereszturi et al. (2016), the pre-eruptive topography covered by a given lava flow
226 was approximated to a planar surface, created from a set of a digitalized rectangular mesh of
227 points along the margins of the lava flow unit, spaced 2 m apart from each other. Height
228 values were extracted from the DEM and assigned to each point, while all points located
229 within the lava flow boundary were subtracted from the mesh. Then, the pre-eruptive surface
230 was modeled by adopting a Triangulated Irregular Network (TIN) surface from the mesh.
231 The Delaunay criterion was applied to maximize the minimum angle of each triangle,
232 avoiding the generation of narrow triangles (Dinas and Bañon, 2014). The recalculated pre-
233 eruptive surfaces possibly present their maximum approximation in case of deeply
234 channelized lava flows, a rather rare case for the selected dataset. Raster images with the pre-
235 eruptive surfaces were generated from the TIN surface, and the average pre-eruptive slopes
236 were measured along the central portion of the lava flows to avoid edge effects. The volume

237 of a given lava flow was calculated as the 3D space enclosed by the modeled pre-eruptive
238 surface and the present topographic surface within the lava flow boundary. Similarly, a
239 thickness map was generated for each lava flow by subtracting the elevation of the pre-
240 eruptive surface from that of the current topographic surface on a cell-by-cell basis. From
241 these data, we computed the maximum thickness of each lava flow and the thickness along
242 the axial profile.

243 We used the deviation from mean elevation (*DEV*) to qualitatively describe the topographic
244 characteristics and roughness pattern of the lava flow surface (De Reu et al., 2013;
245 **Supplementary material 2**). *DEV* measures the relative topographic position of a given cell
246 x_0 by:

$$247 \quad DEV = \frac{z_0 - \bar{z}_n}{\sigma_{z_n}}, \quad (2)$$

248 where $z_0 = z(x_0)$ is the elevation at x_0 , while \bar{z}_n and σ_{z_n} are the mean elevation and the
249 standard deviation of this parameter in the neighborhood of this cell, respectively. In this
250 work, the bandwidth for this calculation was defined using a 5×5 matrix centered at x_0 . A
251 positive *DEV* value indicates that the cell is higher in elevation than the average of its
252 neighbors, whereas a negative value means that the cell elevation is lower than the average
253 elevation in the surroundings (De Reu et al., 2013). Typically, zones with high *DEV* values
254 are recognizable as ridges, levees, or the vent area, while zones with negative *DEV* values
255 are associated with areas close to levees and incisions alongside the front of the main ridges.

256 **3.2.2 Profiles derived from 8-bit grayscale satellite images**

257 Lava flows surface ridges and troughs are easily recognized from satellite images as they are
258 shown as alternating dark and light bands due to regular variations in sun exposure and
259 possibly variable weathering patterns. To assess the surface folding pattern, we introduced a
260 spectral analysis of grayscale data obtained from satellite images (see section 3.2.3). To
261 acquire this data, satellite RGB images (Fig. 1a) for each lava flow were downloaded from
262 the Bing Maps satellite imagery repository with a resolution of 0.26 to 0.28 m/pixel. Satellite
263 images were converted to 8-bit indexed color (Fig. 1b) through the median-cut color

264 quantization algorithm (Heckbert, 1982) using Fiji, an open-source image processing
265 package based on ImageJ (Schneider et al., 2012). The brightness and contrast were adjusted
266 to accentuate features like ridges, as they are observed as dark structures surrounded by
267 lighter ones (Fig. 1b). In the grayscale image, each pixel contains intensity information
268 (amount of light or shades of grays) from 0 to 255. Then, profiles along the flows were drawn,
269 oriented orthogonal to the main structures (to crosscut alternating dark and light zones visible
270 from the satellite images) along the central portion of the flow. The grayscale tone was
271 measured along these profiles considering the mean values within an orthogonal window
272 around the profile to reduce noise in the grayscale profile. The gray intensity measurements
273 were obtained at regular steps throughout the profiles depending on the profile length, with
274 steps varying between 0.96 m (e.g., Putana volcano) and 4.52 m (e.g., Chao dacite).

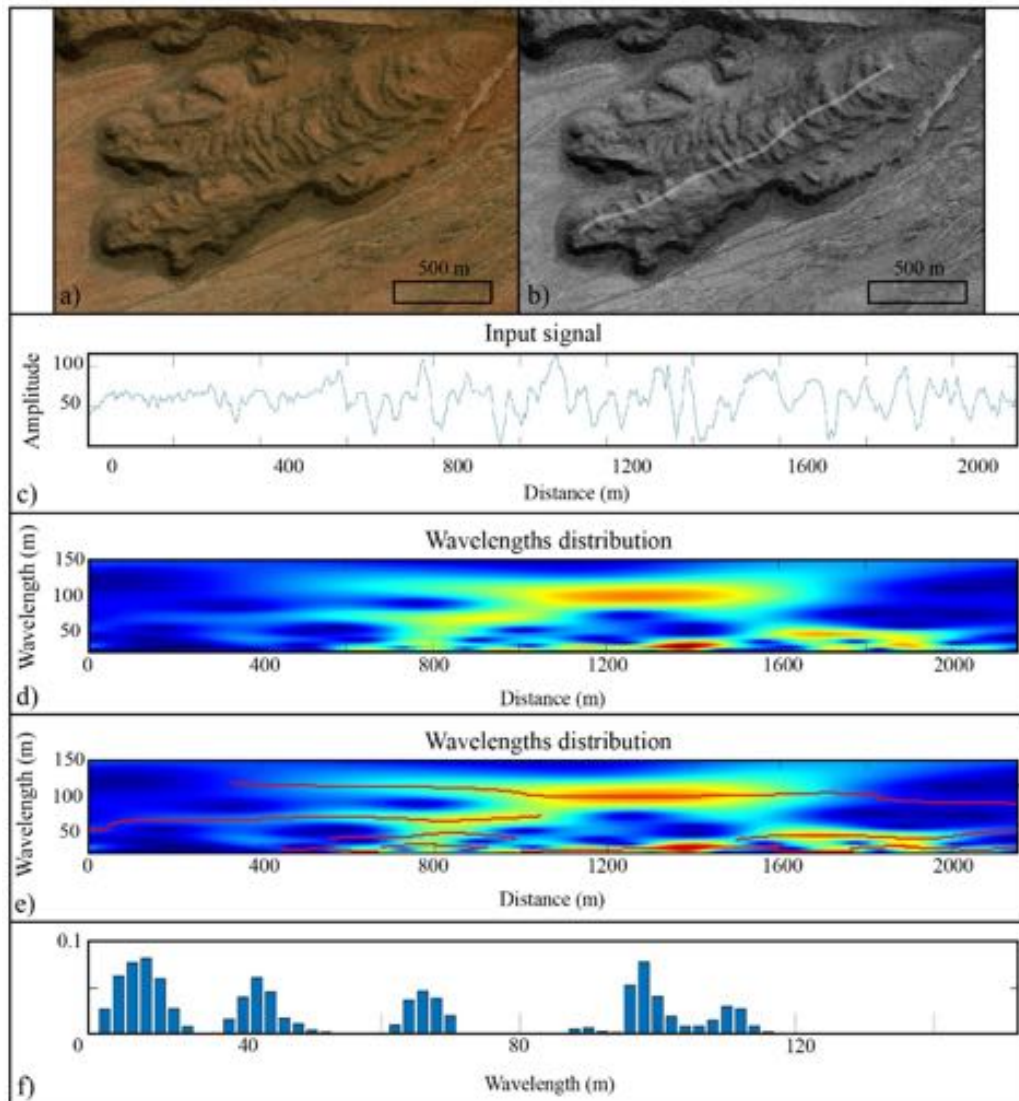
275 **3.2.3 Spectral Analysis and the S-Transform**

276 We analyzed the surface of the lava flows through a spectral analysis of the gray intensity
277 profiles extracted from the 8-bit grayscale images. Surface structures can be in fact, clearly
278 observed in satellite images as light intensity is primarily controlled by surface topography
279 and, possibly, irregularities and weathering patterns. For this reason, the alternation of light
280 and dark areas on the lava flow surface indirectly records the alternation of ridges and troughs
281 on the lava surface, and the distance between two contiguous grey maxima (or minima) is a
282 measure of the wavelength of these undulations.

283 To recognize the presence of repeating patterns along the profiles, we adopted a procedure
284 similar to that described by Lescinsky et al. (2007), who analyzed digital elevation profiles
285 along the flows using a localized Fourier transform, called *S-transform*. The S-transform is
286 a spectral analysis method that allows determining the dominant frequencies locally in
287 sinusoidal signals, thus providing useful information for identifying local structures and the
288 wavelength of repeating patterns. This technique combines elements of wavelet transforms
289 and short-time Fourier transform and has been widely adopted for spectral analysis
290 (Stockwell et al., 1996; Stockwell, 2007).

291 Using this technique, Lescinsky et al. (2007) identified different classes of structures at the
292 Medicine Lake dacite flow (Northern California, USA). A key difference between the
293 technique presented by Lescinsky et al. (2007) and our procedure is the nature of the starting

294 data. While Lescinsky et al. (2007) analyzed elevation data profiles, we studied gray intensity
295 profiles derived from satellite images, focusing our analysis only on the wavelength of the
296 observed light-dark alternations. This necessarily translates to some adaptations of the
297 procedure, as described below.



298
299 **Figure 1.** Ollagüe S lava flow S-Transform spectral analysis. a) Satellite RGB image. Ridges are
300 recognizable as structures transverse to flow direction. b) 8-bit grayscale image. Ridges are
301 represented as black structures surrounded by lighter zones. The white line indicates the studied
302 profile. c) Normalized and detrended grayscale-derived data measured along the surface profile. d)
303 S-Transform spectral analysis. Dark red and yellow zones correspond to high coherence areas, while
304 dark blue zones correspond to lower coherence areas. Coherence represents the quality of fit for a
305 given wavelength (or frequency) at a given location. In other words, a high coherence zone identifies

306 the presence of a dominant wavelength in the input signal at a given segment of the studied profile.

307 e) Equivalent to panel d but including the identification of wavelengths with lateral continuity. f) Bar
308 plot of the dominant wavelengths.

309 For each lava flow, the starting dataset is represented by a profile with values of gray intensity
310 sampled at regularly spaced nodes (Fig. 1c) on satellite images. First, following Lescinsky
311 et al. (2007), detrending and normalization operations were applied to the profiles. This
312 reduces monotonic variations of grey value due to variable luminosity within the satellite
313 images. In particular, the detrending operation consists in subtracting a moving average
314 function from the initial data. The window of this moving average is 700 m, which limits the
315 maximum wavelengths that the procedure is able to identify in the studied lava flows. Note
316 that the shortest lava flow analyzed is about 700 m-long, and thus this value allows us to
317 apply a common detrending strategy for the whole dataset (obviously, the effect of the
318 detrending operation in the shortest lava flows studied is negligible). Then, the S-transform
319 is applied. This provides the local amplitude and local phase spectrum along the profile. The
320 one-dimensional S-transform is named $S(x, \lambda)$, where x is the position along the profile and
321 λ is the wavelength (additional details are presented in Lescinsky et al., 2007, and Stockwell
322 et al., 1996). A high value of $S(x, \lambda)$ is suggestive of a dominant spectral component with a
323 given wavelength λ at the position x along the studied profile. In other words, it suggests the
324 presence of a dominant wavelength λ in the input signal at a given segment of the studied
325 profile (around the position x). The resolvable wavelengths are equal to the profile length,
326 1/2 of the profile length, 1/3 of the profile length and so forth. Thus, spectral resolution is not
327 uniform but increases as the wavelength decreases. We interpolated the values of the
328 spectrum linearly to produce a uniform grid for $S(x, \lambda)$ in both directions (i.e., x and λ ; Fig.
329 1d). Due to resolution limitations and boundary effects, we considered only wavelength
330 higher than 20 m and lower than 1/5 of the profile length. We suggest that such limitation,
331 given the scale of the observed surface structures as well as the general thickness, length, and
332 width of the observed lava flows, does not reduce the ability of the method to identify and
333 measure the first-order structures of the lava flows.

334 Because the absolute values of $S(x, \lambda)$ are also controlled by amplitude, they tend to be higher
335 for structures characterized by long wavelengths. Thus, in addition to the absolute values of

336 $S(x, \lambda)$, structure identification should consider the relationship between $S(x, \lambda)$ at a specific
 337 point and the surrounding values, which are characterized by similar wavelengths.
 338 Accordingly, considering fixed positions along the profile (x_i), our code selects all the
 339 relative maxima of the vectors $\vec{S}_{x_i} = S(x_i, \lambda)$, which are candidates to capture the wavelength
 340 of the dominant structures. From this operation, we obtain a set of positions (x_j, λ_j) which
 341 were clustered to identify continuous bands or patches with high values of $S(x, \lambda)$ and to
 342 discard isolated relative maxima, unable to capture the general characteristics of the flow
 343 (see Fig. 1e, where we illustrate the persistency of a given wavelength along the flow).
 344 Finally, considering only the identified maxima with lateral continuity (red lines in Fig. 1e),
 345 for each value of λ in the matrix $S(x, \lambda)$, we compute:

$$346 \quad I_S(\lambda_0) = \sum_{j=1}^N S(x_j, \lambda_j) \varphi_{\lambda_0}(\lambda_j) \quad (3)$$

347 where $\varphi_{\lambda_0}(\lambda_j) = 1$ when $\lambda_j = \lambda_0$ and $\varphi_{\lambda_0}(\lambda_j) = 0$ when $\lambda_j \neq \lambda_0$. Thus, the function I_S is a
 348 measure of the relevance of the different wavelengths in the studied spectrum. Normalized
 349 bar plots show the smoothed results of I_S and allows identifying the dominant wavelengths
 350 in the grayscale profile (Fig. 1f).

351 3.2.4 Shape analysis of lava flow

352 To characterize and quantify the shape of the lava flow boundaries, we adopted a Fourier
 353 Descriptors (FD) method. The FD method has been widely used in biology, engineering,
 354 computer sciences, sedimentology, and paleontology to describe the shape of different
 355 objects. However, it has never been used to **classify describe** lava flows according to their
 356 morphology. The FD are obtained from the Fourier coefficients of a function that describes
 357 the shape of the lava flow outline as a polygon of N points ($x(a), y(a)$), with $a = 1, \dots, N$.
 358 Each pair of coordinates is transformed in the complex number $z(a) = x(a) + y(a)i$, and
 359 the FD coefficients $c(k)$ of the Fourier Transform of z are given by:

$$360 \quad c(k) = \frac{1}{N} \sum_{a=1}^N z(a) \exp\left(-2\pi i \frac{k}{N} a\right), \quad k = 1, \dots, N \quad (4)$$

361 The $c(k)$ descriptors measure the frequency content of the curve. The first values of k
 362 describe low-frequency information and hence the overall shape of the object (in our case,

363 the lava flow lobe), while higher frequencies record more detailed information about the
364 high-frequency roughness of the object contour. A detailed description of the FD method is
365 provided in Persoon and Fu (1977) and Glasbey and Horgan (1995).

366 Based on the Fourier Descriptors, we defined the variable $P(k)$ as:

$$367 \quad P(k) = \frac{P_k}{P_0} \quad (5)$$

368 where P_k is the perimeter of the lava flow computed at a particular FD coefficient and P_0 is
369 the real perimeter of the lava flow as measured directly on the satellite image. We performed
370 the analysis from $k = 1$ until $k = 14$ for each lava flow. The value of $P(k)$ from 0 to 1,
371 quantifies the perimetral complexity of the lava flow and increases monotonically with k . At
372 a given k , lower values of $P(k)$ reflect a more complex shape of the lava flow, while higher
373 values of $P(k)$ typically reflect simpler external morphologies. To quantify the complexity
374 of the lava flow outline, we selected the values of k at which $P(k)$ exceeds 0.95.

375 **3.3 Lava flow viscosity modeling**

376 The apparent viscosity was modeled for a subset of 14 lava flows with available information
377 about composition and crystal content. Magma rheology does not depend only on the
378 chemical composition of the melt, but also on the relative abundance and physical
379 characteristics of the dispersed phases (crystals and bubbles). The apparent viscosity (η_{app})
380 of a polydisperse mixture of particles in a liquid phase is defined as a function of the viscosity
381 of the melt (η_{melt}) and the relative viscosity (η_r) at a given particle volume fraction ϕ by:

$$382 \quad \eta_{app} = \eta_{melt} \eta_r(\phi). \quad (6)$$

383 The viscosity of the residual liquid is controlled by temperature and composition. We
384 calculated these parameters using the rhyolite-MELTS software (Gualda et al., 2012), trying
385 to fit the known composition and crystallinity. The underlying assumption is that phenocrysts
386 are formed in the magma reservoir at pre-eruptive thermodynamic conditions, whereas
387 microlite crystallization occurred during magma ascent, eruption, and subsequent flow
388 emplacement mainly driven by volatiles loss (Swanson et al., 1989; Cashman and Blundy,
389 2000; Chevrel et al., 2013). The bulk-rock composition was considered representative of the
390 pre-eruptive composition in the magma reservoir, at 1 kbar, 2.5 vol.% H₂O, and an oxygen

391 fugacity controlled by a Quartz-Fayalite-Magnetite buffer. The crystallization of microlites
392 was modeled using the residual melt composition and temperature by decreasing the pressure
393 from 1 kbar to 1 bar under isothermal conditions (simulating magma ascent). The final
394 isobaric crystallization stage is calculated at 1 bar from the liquidus temperature until the
395 solidus temperature is reached. The assumption of a 2.5 vol.% H₂O content may be an
396 inherent limitation of the viscosity calculation; however, the presence of amphibole (typically
397 observed in these lavas; e.g. Chao, Chac-Inca, Llullaillaco, Lastarria, Guallatiri, Uturuncu)
398 indicates hydrous conditions, and the assumed water content is in agreement with that
399 reported by De Silva et al. (1994) for the Chao dacite and in the range of glass inclusions
400 from the Uturuncu volcano obtained by Sparks et al. (2008).

401 The viscosity of the interstitial melt was calculated following Giordano et al. (2008). This
402 model was used because it has been successfully used for intermediate to silicic flows (Sato
403 et al., 2013; Latutrie et al., 2017; Reyes Hardy et al., 2021) and, unlike to other viscosity
404 calculators (e.g. Bottinga and Weil, 1972; Shaw, 1972), it considers the non-Arrhenian T-
405 dependence of viscosity by the Vogel-Fulcher-Tammann equation:

$$406 \quad \log \eta_{melt} = A + \frac{B}{T-C} \quad (7)$$

407 where A, B, and C are composition-dependant parameters and T is temperature (Giordano et
408 al., 2008).

409 It is well-known that the relative viscosity η_r depends on the volumetric abundance, aspect
410 ratio, crystal size distribution and shape of the crystalline phases, the strain rate of the flow,
411 vesicularity, and bubble content (Castruccio et al., 2010; Cimarelli et al., 2011, Mueller et
412 al., 2011; Chevrel et al., 2013, Klein et al., 2017, 2018). However, due to the lack of a robust
413 dataset for the analyzed lava flows, we assumed a bubble-free interstitial liquid with bimodal
414 crystal size and shape distribution.

Flow	Type (this work)	Maximum wavelength (m)	Second maximum wavelength (m)	Λ	Thickness (m)	Runout (km)	Width (m)	Pre-eruptive slope (°)	SiO ₂ (wt%)	Cxs (wt%)	P _k > (95)	Vol (km ³)	Yield Strength (MPa)	Effusion rate (m ³ s ⁻¹)	Area (km ²)	Reference
Acotango	Ridged	141	84	1.6	236	6.17	2292	16.66	-	-	6	0.78	632	203.41	8.66	-
Cerro Bayo	Ridged	228	142	1.6	173	3.45	1571	20.98	-	-	5	0.34	598	139.17	5.05	-
Cerro Bayo	Ridged	244	169	1.4	210	3.86	1582	28.07	66.53	-	4	0.32	993	178.53	3.72	Naranjo et al. (2013)
Chao	Ridged	274	244	1.1	344	14.27	7239	11.65	68.28	48	7	9.25	768	170.17	59.61	de Silva et al. (1994)
Ollagüe NW	Ridged	90	71	1.2	132	3.29	1183	32.75	63.26	43	3	0.13	712	130.04	2.48	Mamani et al. (2008)
Acomarachi	Coulee	120	84	1.4	103	2.95	2306	13.3	-	-	7	0.22	167	0.48	7.35	-
Colaichi	Coulee	94	53	1.7	85	1.77	1396	20.74	-	-	5	0.06	253	1.68	2.20	-
Chac-Inca W	Coulee	106	96	1.1	180	2.85	2596	15.68	67.04	45	5	0.55	577	20.00	6.31	Selles and Gardeweg (2018)
Chac-Inca E	Coulee	93	70	1.3	144	1.30	1310	18.25	-	45	2	0.12	468	10.67	2.02	Selles and Gardeweg (2018)
Ollagüe N	Coulee	*	*	*	196	2.00	1608	20.48	64.49	30	2	0.17	659	29.78	2.15	Feeley et al. (1993)
Llullaillo	Leveed	146	102	1.4	164	5.32	3475	30.57	65.83	17	*	0.27	720	206.54	4.68	Gardeweg et al. (1984)
Olca-Paruma	Leveed	88	65	1.3	81	2.44	847	14.1	63.06	33	5	0.05	210	19.92	1.31	Martinez (2019)
Tata Sabaya	Leveed	215	142	1.5	125	3.82	886	31.68	-	-	4	0.15	759	221.87	2.46	-
Tata Sabaya	Leveed	97	56	1.7	120	3.51	853	34.84	61.11	-	4	0.08	580	77.04	1.98	de Silva et al. (1993)
Sairecabur N	Leveed	85	50	1.7	54	1.59	633	14.91	61.20	-	7	0.01	118	3.34	0.64	Mamani et al. (2010)
Putana SW	Leveed	78	35	2.2	70	1.80	813	26.88	-	-	4	0.02	266	14.01	0.96	-
Falso Azufre	Leveed	66	44	1.5	122	4.04	995	16.62	-	-	5	0.09	220	18.62	2.74	-
Irruputuncu	Leveed	153	110	1.3	100	2.72	958	27.77	59.72	27	2	0.06	306	19.87	2.13	Rodriguez et al. (2015)
Irruputuncu	Leveed	70	44	1.5	167	1.51	865	36.67	62.40	27	2	0.06	987	327.97	0.95	Wörner et al. (1992)
Llullaillo	Leveed	70	41	1.7	152	3.33	928	43.88	65.42	30	2	0.10	712	70.59	2.34	Gardeweg et al. (1984)
Putana S	Leveed	58	45	1.3	77	1032	690	32.9	-	-	3	0.01	339	17.93	0.55	-
Condor	Leveed	118	82	1.4	92	4.67	799	22.22	65.2	-	5	0.06	213	10.56	2.44	Grosse et al. (2018)
Socompa S	Leveed	*	*	*	210	5.11	1643	16.52	-	-	5	0.49	516	242.34	6.59	-
Lascar N	Leveed	98	60	1.6	93	4.15	836	25.03	63.97	-	6	0.08	388	50.73	2.22	Gardeweg et al. (2011)
Socompa	Leveed	*	*	*	106	3.99	1021	30.02	-	-	5	0.11	420	42.82	3.07	-

Flow	Type (this work)	Maximum wavelength (m)	Second maximum wavelength (m)	Λ	Thickness (m)	Runout (km)	Width (m)	Pre - eruptive slope (°)	SiO ₂ (wt%)	Cxs (wt%)	P _k > (95) (km ³)	Vol (km ³)	Yield Strength (MPa)	Effusion rate (m ³ s ⁻¹)	Area (km ²)	Reference
San Pedro N	Breakout	285	257	1.1	139	564	1533	14.35	64.00	28	13	0.27	299	8.86	5.51	Bertin and Amigo (2019)
San Pedro NW	Breakout	220	137	1.6	151	564	2415	9.78	65.5	23	14	0.51	269	7.98	7.89	Bertin and Amigo (2019)
Isluga	Breakout	120	66	1.8	72	564	1117	11.67	58.72	28	14	0.04	88	0.25	2.04	Cascante (2015)
Guallatiri	Breakout	98	60	1.6	182	564	937	13.82	63.4	35	8	0.12	472	35.65	1.54	Sepulveda et al. (2020)
Licancabur N	Breakout	74	53	1.4	59	564	726	16.72	60.5	< 12	14	0.04	181	1.78	1.40	Figuroa et al. (2009) Mamani et al. (2010)
Licancabur M	Breakout	78	40	1.9	54	564	896	16.9	59.60	< 12	14	0.04	179	1.71	1.47	Mamani et al. (2010)
Licancabur S	Breakout	126	100	1.2	115	564	950	12.08	60.20	< 12	12	0.15	246	5.50	3.02	Mamani et al. (2010)
San Pedro W	Breakout	90	58	1.5	79	564	705	19.87	62.20	-	12	0.07	252	4.17	2.18	Bertin and Amigo (2019)
San Pedro SW	Breakout	111	58	1.9	38	564	903	22.9	62.02	15	12	0.03	155	0.85	1.78	Bertin and Amigo (2019)
Paniri	Breakout	99	57	*	97	564	1316	13.31	-	-	9	0.10	222	3.82	2.54	-
Lastarria N	Breakout	95	80	1.1	109	564	881	11.21	60.41	31	14	0.14	210	3.54	3.27	Naranjo (1992, 2010)
Ollagüe S	Breakout	98	66	1.4	50	564	961	13.18	-	37	14	0.03	101	0.36	1.89	This study
Olca-Paruma W	Breakout	*	*	*	88	564	961	18.29	63.52	30	14	0.10	284	6.38	2.60	Martinez (2019)
Falso Azufre W	Transitional	*	*	*	144	564	1876	13.84	-	-	8	0.21	235	4.41	5.19	-
Lascar S	Transitional	90	53	1.7	75	564	718	23.46	-	-	2	0.03	232	2.76	1.39	-
Uturuncu	Transitional	112	57	1.9	242	564	3781	11.34	65.64	35	14	0.97	244	15.27	19.20	Sparks et al. (2008)
Falso Azufre E1	Transitional	106	87	1.2	94	564	1231	10.19	-	-	5	0.11	162	1.70	2.92	-
Falso Azufre E2	Transitional	138	100	1.3	95	564	1795	9.37	66.80	-	3	0.15	122	0.76	4.81	Grosse et al. (2018)
El Misti	Transitional	120	66	1.8	118	564	720	24.38	60.50	-	5	0.06	304	25.79	2.13	Rivera et al. (2017)
Lastarria SW	Transitional	50	34	1.4	82	564	890	37.16	66.16	26	5	0.01	353	1.83	0.42	Naranjo (1992, 2010)
Aucanquilcha	Transitional	*	*	*	154	564	682	32.81	-	-	4	0.09	169	0.50	1.67	-
Llullaillaco S	Transitional	194	128	1.5	183	564	1649	22.28	65.65	17	14	0.28	576	208.18	4.52	Gardeweg et al. (1984)
El Muerto	Transitional	141	108	*	216	564	1809	10.76	-	-	4	0.41	218	29.70	8.67	-
Sairecabur S	Transitional	74	60	*	91	564	1208	13.61	61.55	-	6	0.01	700	159.09	0.41	Mamani et al. (2010)

415 **Table 2.** Dataset of the studied CVZ lava flows. * = not analyzed, - = not available data, Λ = Maximum
416 wavelength / second maximum wavelength, $P_{k > 95}$ = value of k at which $P(k)$ exceeds 0.95. Cxs =
417 crystallinity; only includes phenocrysts. Thickness, runout, and width refer to maximum values. Yield
418 strength is calculated as a function of thickness, density (2500 kgm⁻³), the gravity acceleration
419 constant (9.81 ms⁻²) and the slope. Effusion rates were obtained following equation 12 (see section
420 5.5). Volcanoes with more than one flow include an abbreviation to differentiate them. N = north, S
421 = south, E = east, NW = northwest, SW= southwest, W = west, E1 = East 1, = E2 = East 2, M = middle,
422 L = lower, U = upper.

423 The effect of the suspended phases was modeled as a mixture of coarse (ϕ_c) and fine (ϕ_f)
424 particles (Farris, 1968; Chevrel et al., 2013) considering that:

$$425 \quad \eta_r = \eta_r(\phi_c) \eta_r(\phi_f) \quad (8)$$

426 Coarse particles were modeled as spheres to mimic the effect of phenocrysts, while fine
427 particles were modeled as needles to mimic the effect of microlites.

428 For calculating η_r , we adopted the rheological model proposed by Costa (2005) and modified
429 by Costa et al. (2009), which is based on a semi-empirical non-Newtonian relationship for
430 dilute-to-highly-concentrated polydisperse suspensions. We adopted this model because it
431 considers the crystal fraction and shape of the particles and, contrary to other methods (e.g.,
432 Krieger and Dougherty, 1959; Pinkerton and Stevenson, 1992), it includes the strain-rate
433 dependency that partially controls the geometrical redistribution of the suspended particles
434 and the non-Newtonian behavior as:

$$435 \quad \eta_r(\phi) = \frac{1 + \phi^\delta}{[1 - F(\phi, \varepsilon, \gamma)]^B \phi^*} \quad (9)$$

$$436 \quad F = (1 - \varepsilon) \operatorname{erf} \left[\frac{\sqrt{\pi}}{2(1 - \varepsilon)} \phi (1 + \phi^\gamma) \right] \quad (10)$$

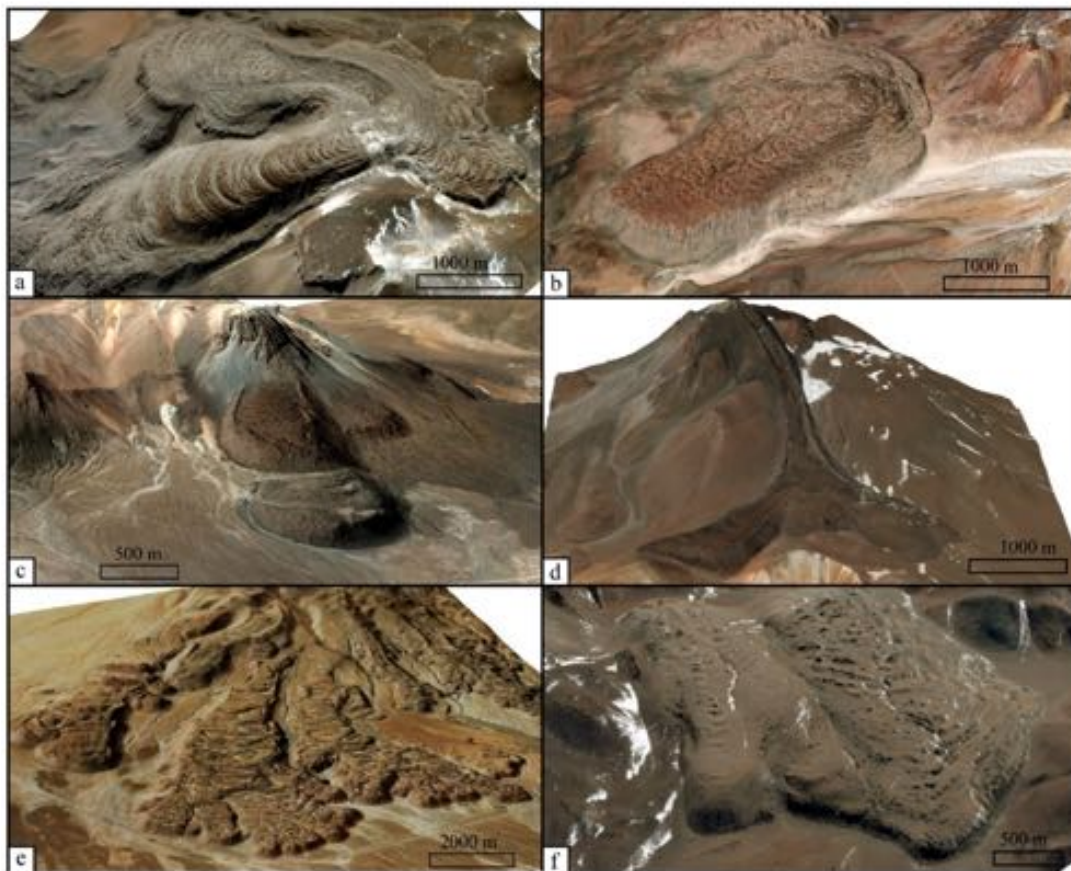
$$437 \quad \phi = \frac{\phi}{\phi^*} \quad (11)$$

438 where ϕ^* represents the critical solid fraction that indicates the transition from a system
439 where the viscosity of the liquid phase controls the viscosity of the suspension to a system
440 where particle-particle interactions induce a strong viscosity increase (Caricchi et al., 2007).

441 The fitting parameters (Supplementary material 3) were extracted from Cimarelli et al. (2011)
442 obtained from analog experiments of polydisperse suspensions of coarse and fine particles at
443 an intermediate strain rate of 10^{-4} s^{-1} .

444 4. Results

445 Based on the general plain-view shape of the flows, thickness distribution, folding patterns,
446 and the presence of distinctive morphological features such as levees, lobes, the position of
447 the vent and surface textures, the 49 lava flows analyzed in this work were classified grouped
448 into four main types: Ridged flows, Coulee lavas, Leveed flows, and Breakout flows (Fig.
449 2). A representative example is shown for each type of lava in Figures 3-7, while all the
450 analyzed flows and their data are presented in the Supplementary material 2. Lava flows with
451 characteristics common to more than one type were categorized as Transitional lavas.



452
453 **Figure 2.** Examples of the main types of flows identified in the CVZ. a) Ridged flow (Bayo N and
454 Bayo S). b) Coulee flow (Chac-Inca W). c) Short leveed flow (Irruputuncu L and Irruputuncu U). d)

455 Long leveed flow (Lullailaco N). e) Breakout flow (San Pedro N, San Pedro NW, and San Pedro
456 W). f) Transitional flows (Falso Azufre E1 and Falso Azufre E2).

457 **4.1 Ridged flows**

458 This group comprises thick, large-volume lava flows with well-exposed and preserved
459 arcuate ridges on the upper surface (Fig. 2a, 3a,c, Supplementary material 1.1). ~~Typically,~~
460 ~~levee structures are not developed, while~~ The flow surface is convex downflow, with long,
461 continuous, and highly curved ridges that span the entire flow (Fig. 3a,c). Lava flow width
462 tends to increase downslope, with the terminal front characterized by a single, sub-rounded
463 lobe. Typically, thickness slightly increases downslope, with the maximum thickness (Table
464 2) located in the central sector of the channel (Fig. 3b,f). On gentle slopes, lava flows and the
465 associated ridges are disposed nearly concentrically around the vent areas, while on zones
466 with steeper slopes ridges only develop downslope..

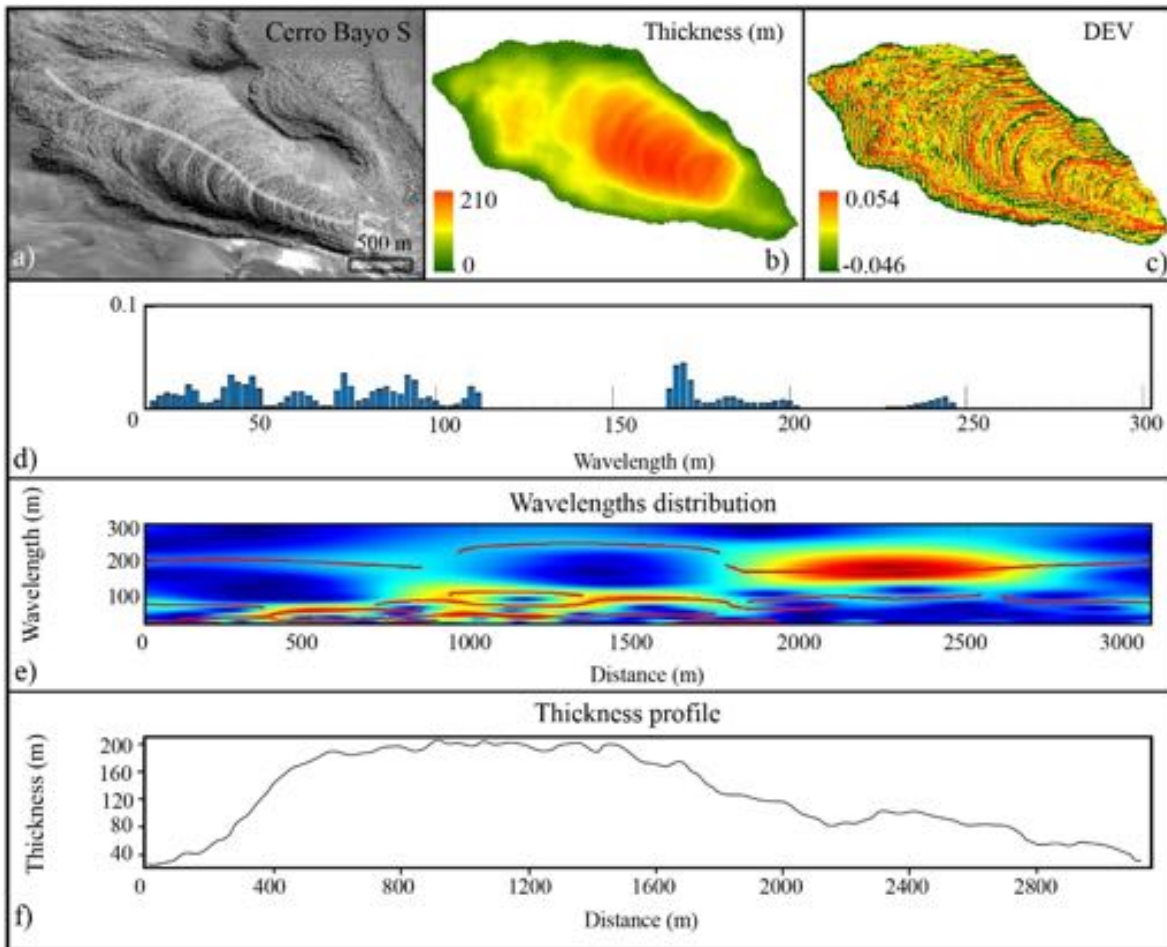
467 In plain view, these flows show relatively simple shapes, with $P(k)$ exceeding 0.95 for values
468 of k between 3 and 7. Typically, surface ridges present the longest dominant wavelengths
469 (Table 3, Supplementary material 2.1), and they span the entire surface continuously (e.g.,
470 Bayo N, Ollagüe NW, Chao dacite, Acotango; Supplementary material 2.1) and have a direct
471 relation with the maximum thickness (Fig. 3e and 3f).

472 ~~In these flows, ridges with small wavelengths (20—50 m; Fig. 3f, Supplementary material~~
473 ~~2.1) span the entire surface intermittently. Longer wavelengths, which are related to multiple~~
474 ~~trains of folds, occur discontinuously along the entire axial profile, while the second longest~~
475 ~~wavelength (71—244 m; Table 2, Supplementary material 2.1) in the ridge spacing is~~
476 ~~continuous but does not span over the entire surface. Typically, these flows present the~~
477 ~~longest dominant wavelengths (90—274 m; Table 2, Supplementary material 2.1) that span~~
478 ~~the entire surface continuously (e.g., Bayo N, Ollagüe NW, Chao dacite, Acotango;~~
479 ~~Supplementary material 2.1). In the Bayo S lava flow, the longest wavelength does not occur~~
480 ~~continuously along the surface, but it is mainly confined to the medial zone, suggesting a~~
481 ~~direct relation with the maximum thickness (Fig. 3e and 3f).~~

482 **4.2 Coulee flows**

483 This group consists of lobulated lava flows with rough upper surfaces (Fig. 2b, 4a,c,
484 Supplementary material 1.2). Widths and lengths tend to be similar, while flow thickness
485 progressively decreases downslope (Figs. 4b,f). These lavas are emplaced on medium slopes
486 ~~from 13° to 21°~~, with initial stages of growth associated with extrusion from a vent possibly
487 sited on a sub-horizontal topography. Ridges in the vent area initially form continuous and
488 concentric structures that progressively increase in width with distance. The ridges, which
489 are convex downflow ~~and concentric around the vent~~, are irregularly spaced and span the
490 entire flow. They are generally laterally discontinuous, being mainly formed by the alignment
491 of small, elongated mounds. ~~Distal zones of the rear vent area exhibit disaggregated ridges~~
492 ~~and isolated crumble breccias.~~

493 In plain view, these lavas exhibit simple morphologies, with P values above 0.95 at k values
494 from 1 to 7. The maximum dominant wavelength of surface ridges typically occurs
495 continuously only in medial sectors (Fig. 4e; Table 3, Supplementary material 2.2). The
496 absence of a direct relationship between maximum thickness and maximum wavelength (Fig.
497 4e,f, Supplementary material 2.2) in this group may be due to an initial formation of
498 concentric and tight ridges close to the vent area related to the extrusion itself. During lava
499 emplacement, gravitational forces become dominant and control the propagation of the flow,
500 extending the lava downslope with a subsequent elongation of surface ridges in this direction.



501

502 **Figure 3.** Diagram with the analyses performed on the Bayo S ridged flow. a) the grayscale satellite
 503 image. b) thickness map. c) DEV map shows prominent ridges and steep edges as red zones. -d) bar
 504 plot of the dominant wavelengths. e) S-Transform spectral analysis. f) thickness axial profile. The
 505 white line in the grayscale image represents the profile along which the spectral, thickness and slope
 506 analyses were performed.

507 ~~Folds and ridges with small wavelengths occur discontinuously along the surface of all flows.~~
 508 ~~They are observed on proximal to medial sectors and may be related to crumble breccias or~~
 509 ~~spines scattered on ridges peaks. The wavelength of these structures is often largely dispersed~~
 510 ~~(Fig. 4d) and may be associated with heterogeneous and discontinuous structures. They are~~
 511 ~~mainly located in medial sectors, although they are also present in proximal and distal zones.~~
 512 ~~The second longest wavelengths (53–96 m, Table 2) are discontinuously present along the~~
 513 ~~entire flows, while the maximum dominant wavelength in each flow (93–120 m; Table 2,~~
 514 ~~Supplementary material 2.2) typically occurs continuously only in medial sectors (Fig. 4e).~~
 515 ~~Overall, the analyzed lavas of this type present the smallest difference between the maximum~~

516 ~~dominant wavelength values. The absence of a direct relationship between maximum~~
 517 ~~thickness and maximum wavelength (Fig. 4e,f, Supplementary material 2.2) in this group~~
 518 ~~may be due to an initial formation of concentric and tight ridges close to the vent area related~~
 519 ~~to the extrusion itself. During lava emplacement, gravitational forces become dominant and~~
 520 ~~control the propagation of the flow, extending the lava downslope with a subsequent~~
 521 ~~elongation of surface ridges in this direction.~~

522 **Table 3.** Main wavelengths identified using the S-Transform spectral analysis for the
 523 different types of lavas.

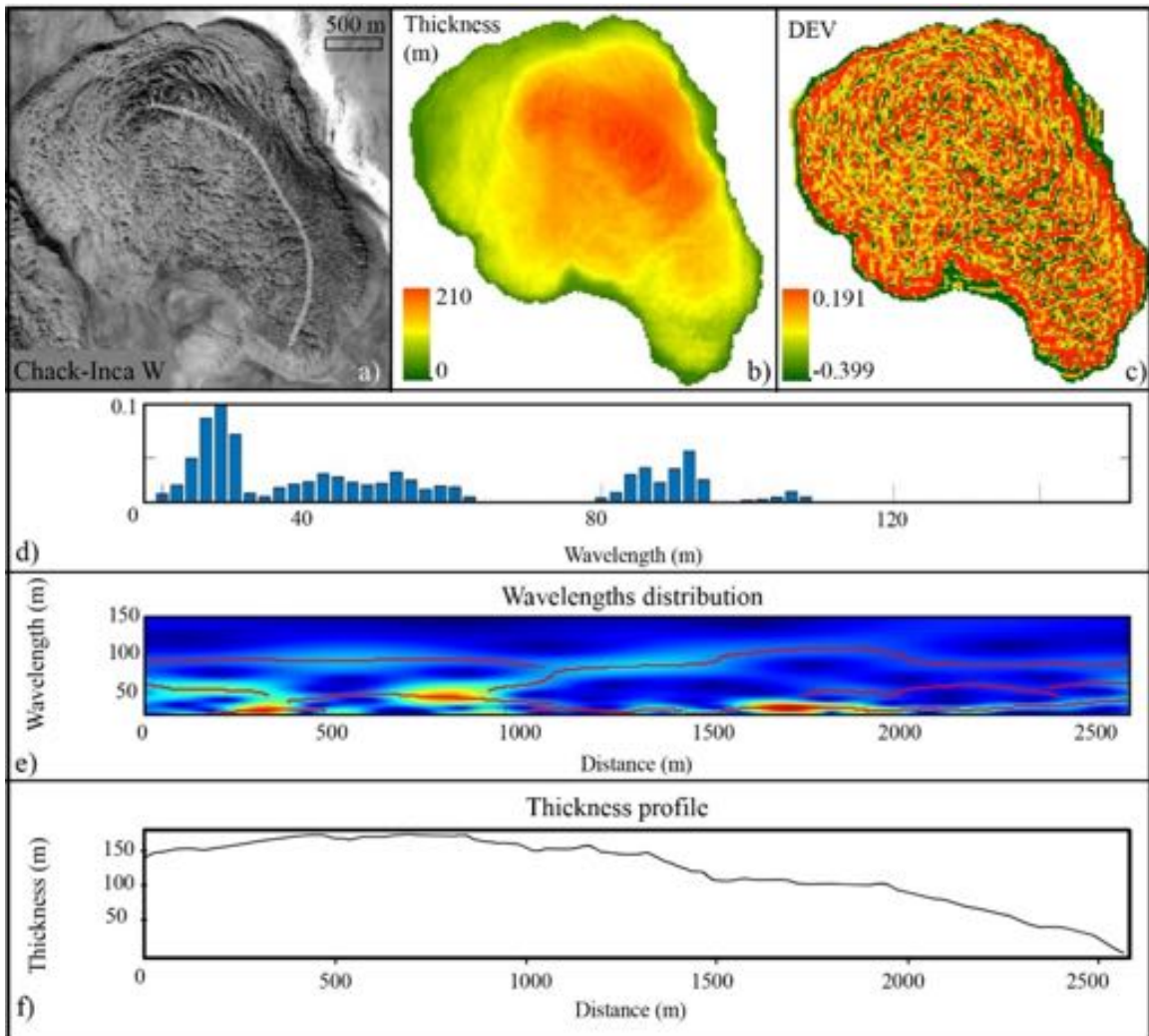
Type	First generation of folds	Second maximum dominant wavelength	Maximum dominant wavelength
Ridged	Intermittent along the flow surface	Continuous but not over the entire surface (71 – 244 m)	Continuous along the entire surface. Spatially related to maximum thickness (90 – 274 m)
Coulee	Typically on proximal to medial sectors related to crumble breccias or spines	Discontinuously present along the entire surface (53 – 96 m)	Continuously only in medial sectors (93 – 120 m)
Leveed	Discontinuous along the entire flow	Typically only in medium sectors (41 -142 m)	Spatially related to the thickness. Continuous on zone of maximum thickness (58 – 215)
Breakout	Discontinuous mainly in medial-to-distal zones	Spatially related to the thickness distribution.	Spatially related to the thickness distribution. Continuous along the surface for thick flows (98 285 m) and typically only in medial to distal zones for thin flows with a thicker front (74 – 111 m)

524

525 **4.3 Leveed flows**

526 This group corresponds to lava flows with rough surfaces, well-exposed levees that form a
 527 clear channel, and moderately preserved surface ridges (Figs. 2c,d, 5a,c). Maximum widths
 528 of these lava flows generally develop into the frontal sector, where they considerably exceed
 529 average flow widths. Thickness significantly increases downslope (Figs. 5b,f), generally
 530 reaching the maximum value at the flow front (Table 2). However, in some cases, thickness
 531 remains virtually constant downstream (Supplementary material 2.3).

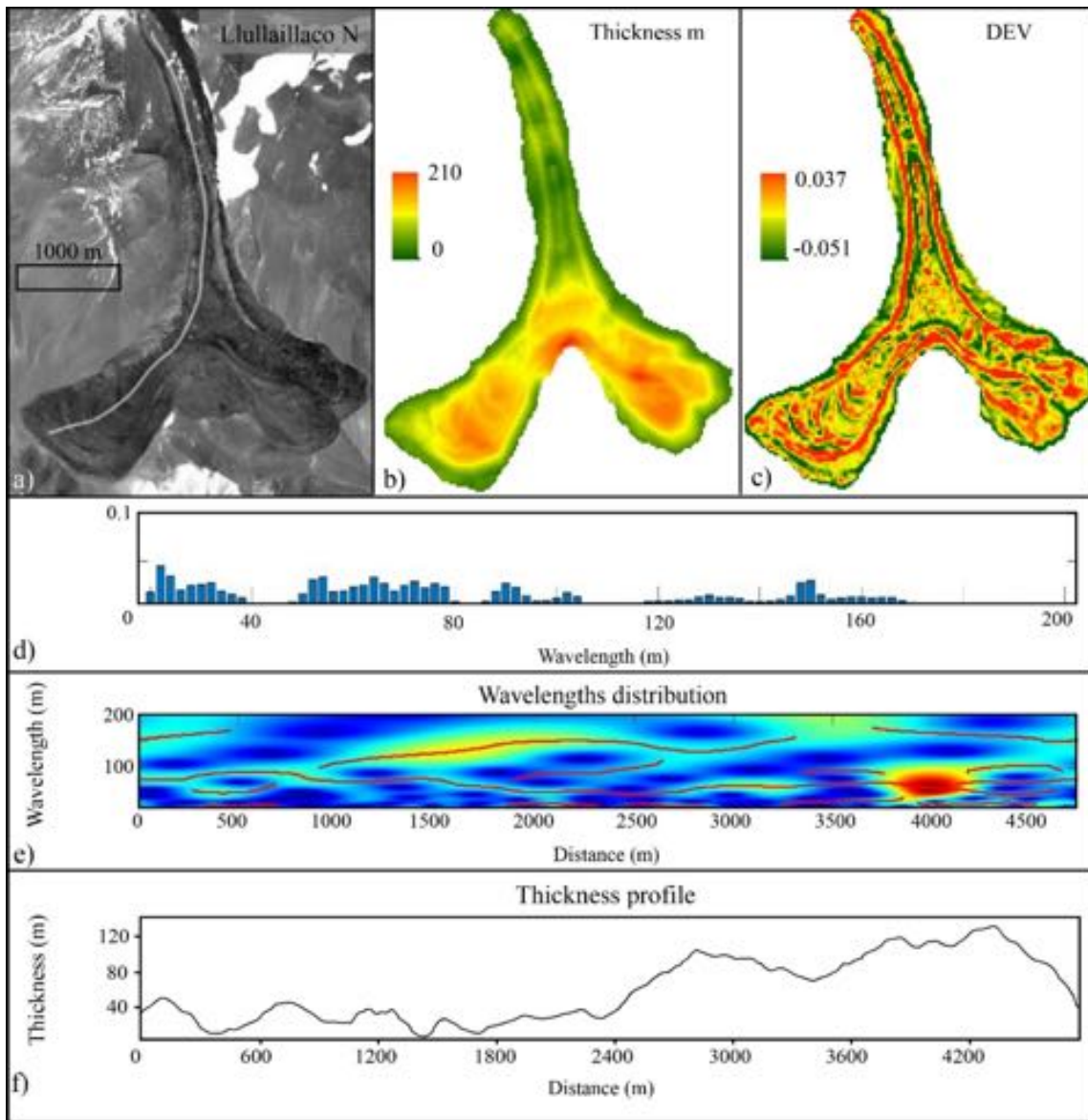
532 Lava flows from this group present variable runouts. The underlying slope varies
533 considerably between proximal ($\sim 34^\circ$) and distal areas ($\sim 14^\circ$) in long flows, while only steep
534 slopes ($> 30^\circ$) were observed in short flows (Table 2). Lavas are highly channeled, with well-
535 formed levees in proximal-to-medial zones. Minimum channel width tends to decrease with
536 slope. Surface ridges are moderately curved, convex to downflow, and span over the central
537 portion of the flow channel. Generally, the ridges of long flows range from densely
538 developed, regularly spaced ridges of decametric size and moderate curvature (medial-to-
539 proximal zones; e.g., Olca-Paruma M, Supplementary material 1.3), to 100 m-height ridges,
540 irregularly spaced, and with low curvature and density, which are recognized in medial-to-
541 distal zones. In the shortest flows, the surface ridges are densely developed and are present
542 along the entire flow.



544 **Figure 4.** Diagram with the analyses performed on the Chack-Inca W coulee flow. a) grayscale
545 satellite image. b) thickness map. c) DEV map. Ridges and mounds are radially distributed around
546 the vents, while they tend to be transversal to flow direction in distal areas. e) bar plot of the dominant
547 wavelengths. f) S-Transform spectral analysis. h) thickness axial profile. The white line in the
548 grayscale image represents the profile along which the spectral, thickness and slope analyses were
549 performed.

550 In plain view, leveed flows show a simple shape, with $P(k)$ values rapidly exceeding 0.95.
551 Overall, short leveed flows have simpler shapes, reaching values of $P(k)$ of 0.95 at k values
552 from 2 to 3, while long leveed flows reach $P(k) = 0.95$ at k values from 4 to 7. The maximum
553 dominant wavelength spatially correlates with thickness (Table 3). Lavas with thickness
554 increasing downslope (e.g., Lullaillaco N, Falso Azufre M, Irruputuncu L, Lullaillaco U,
555 Putana SW flows, Fig. 5, Supplementary material 2.3) present their maximum dominant
556 wavelengths only on medial-to-distal sectors (Fig. 5e), while lavas without significant
557 thickness variations show continuous dominant wavelenghts (Tata Sabaya volcano,
558 Supplementary material 2.3)

559



560

561 **Figure 5.** Diagram with the analyses performed on the Lulluillaco N long leveed flow. a) grayscale
 562 satellite image. b) thickness map. c) DEV map showing levees and prominent ridges in the frontal
 563 zone clearly identifiable as high DEV zones. d) bar plot of the dominant wavelengths. e) S-Transform
 564 spectral analysis. f) thickness axial profile. The white line in the grayscale image represents the profile
 565 along which the spectral, thickness and slope analyses were performed.

566 ~~In these lavas, small wavelength ridges are not continuous and occur along the entire flow.~~
 567 ~~Subsequently, longer wavelengths, mainly related to folding trains, span the entire surface~~
 568 ~~intermittently (Fig. 5e), while the second longest wavelength (41—142 m; Table 2) typically~~
 569 ~~occurs only in the medium sector of the axial profile. The maximum dominant wavelength~~

570 ~~(58—215 m; Table 2) generally increases with lava flow thickness (Fig. 5e,f). Lava flows~~
571 ~~without significant thickness variations show spectral analyses with continuous and~~
572 ~~homogeneous wavelengths within high coherence zones, generally spanning the entire flow~~
573 ~~(e.g., Tata Sabaya volcano, Supplementary material 2.3). On the other hand, lava flows in~~
574 ~~which thickness increases downslope (e.g., Lullailaco N, Falso Azufre M, Irruputuncu L,~~
575 ~~Lullailaco U, Putana SW flows, Fig. 5, Supplementary material 2.3) exhibit zones with~~
576 ~~highly coherent wavelengths located only on medial to distal sectors (Fig. 5e).~~

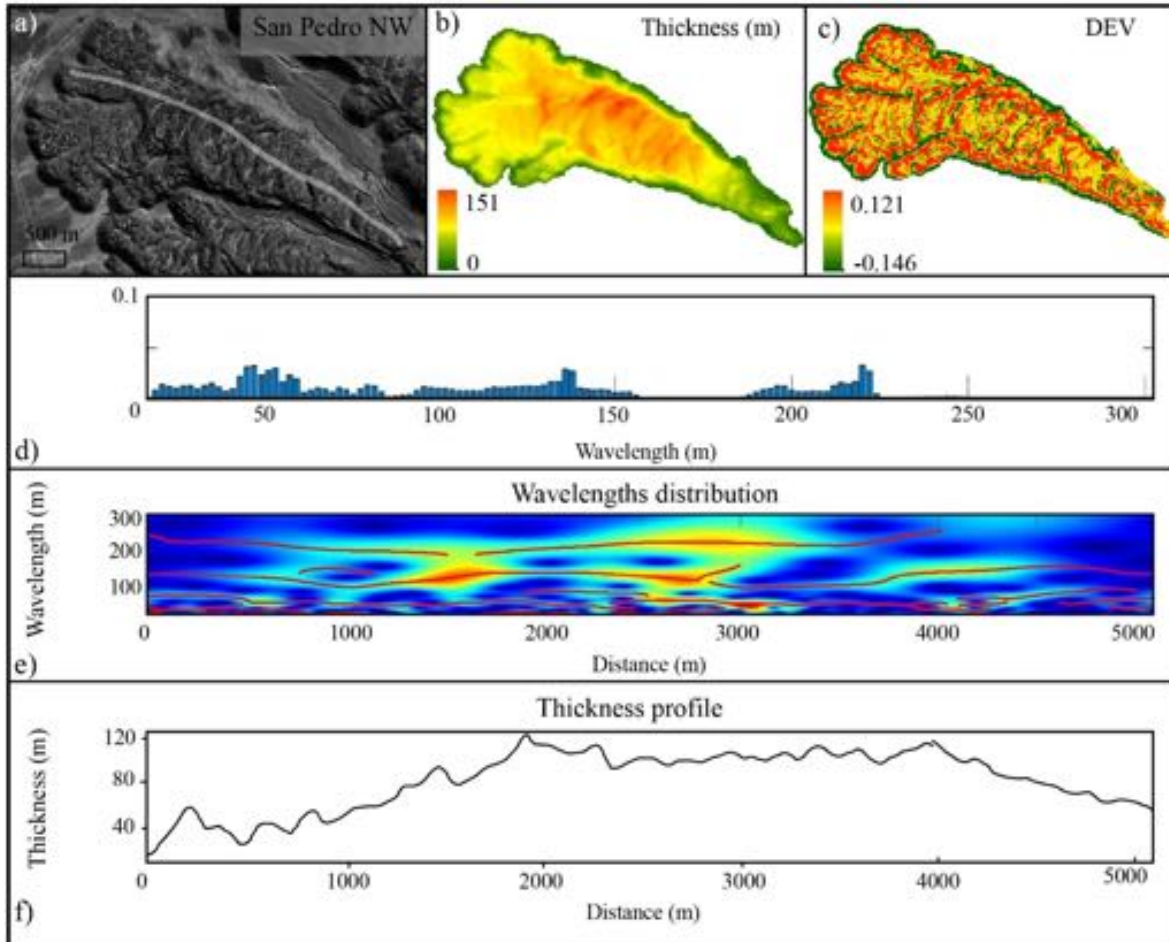
577 **4.4 Breakout flows**

578 This group corresponds to lava flows characterized by a surface with wide-to-braided ridges
579 and multiple lateral and frontal lobes (Fig. 2e, 6a). In proximal zones, lateral margins vary
580 from nearly linear to irregular with constant width, while flows enlarge toward distal areas,
581 presenting multiple lobes and branched structures. These lava flows ~~are characterized by~~
582 **present** discontinuous, narrow, and irregular levee structures that delimit a central channel,
583 **while** ~~and by~~ convex ~~surface~~ ridges ~~spanning~~ the entire channel. Ridges **are** orthogonal to the
584 flow direction, with irregular spacing and height. These lavas occur on gentle to medium
585 slopes, and their morphologies and deformation patterns are not controlled by flow thickness.

586 Two families of breakout flows can be recognized based on thickness. Thick breakout flows
587 have wide, straight, and cusped ridges, generally spaced by deep troughs that span the entire
588 channel width (Fig. 6a,c). The thickness (~ 130 m) does not significantly vary downslope,
589 with maximum thicknesses and cusped ridges generally occurring in correspondence with
590 the central channel (Fig. 6b,f). In general, lobes are poorly developed and only occur as lateral
591 structures. On the other hand, thin breakout flows have abundant, low amplitude and curved,
592 braided ridges (Figs. 7a,c). Levee structures are common and more developed respect to
593 thicker flows, while the maximum thickness (~ 75 m) tends to increase downslope (Figs.
594 6b,f). However, some of these flows also present virtually constant thickness with distance
595 from the vent. Ridges show a braided aspect with breakouts and overflow widely developed
596 along the lateral and frontal margins.

597 In plain view, these flows show the more complex morphologies, with P(k) values of 0.95 at
598 k from 8 to 14. Overall, thin flows have more complex shapes than thick ones. ~~which is~~

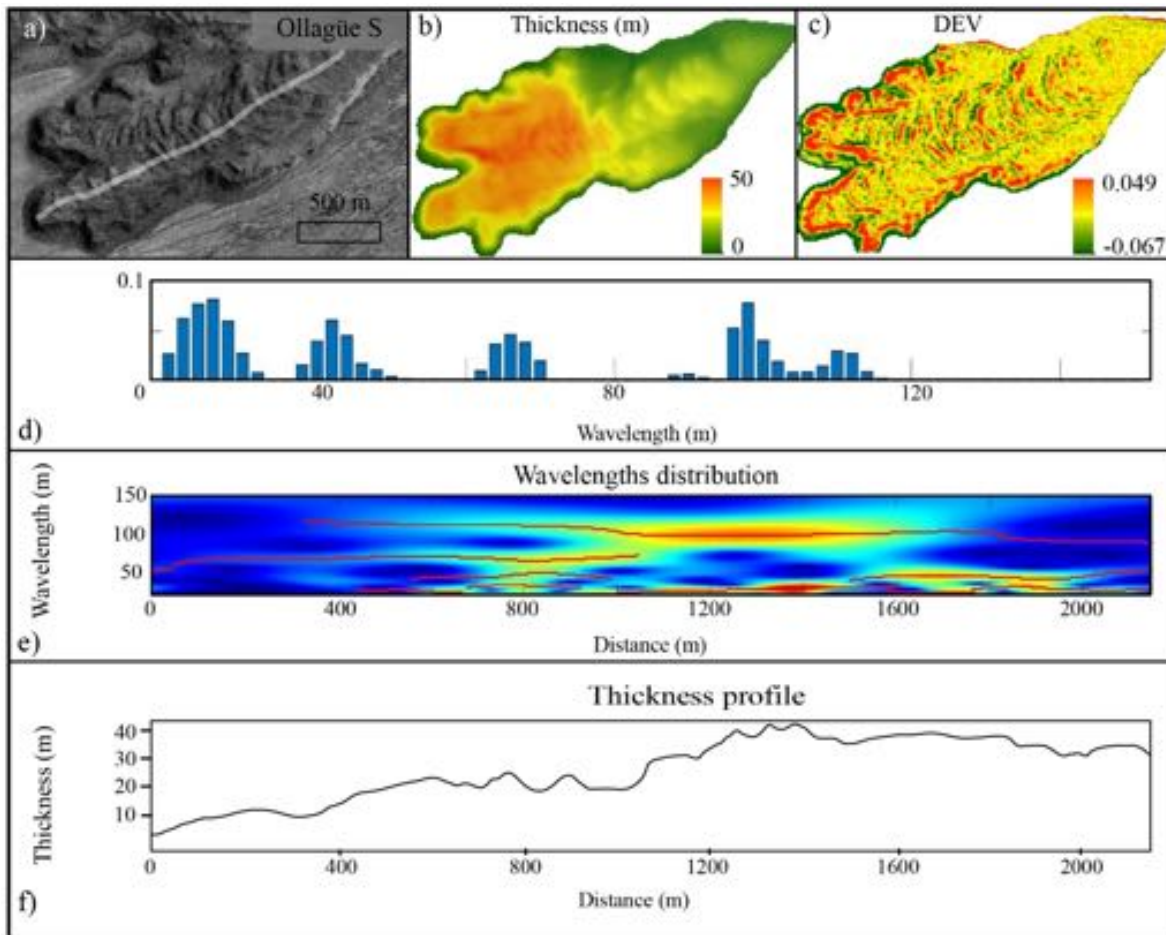
599 ~~related to the vast development of lateral and frontal breakout structures.~~ Thin and thick
 600 breakout flows show a similar folding pattern, suggesting a direct relationship between
 601 thickness and the spatial distribution of the maximum dominant wavelength.



602
 603 **Figure 6.** Diagram with the analyses performed on the San Pedro NW thick breakout flow. a)
 604 grayscale satellite image. b) thickness map. c) DEV map showing prominent ridges, steep edges, and
 605 the intersection between breakouts mainly in the front. e) bar plot of the dominant wavelengths. f) S-
 606 Transform spectral analysis. h) thickness axial profile. The white line in the grayscale image
 607 represents the profile along which the spectral, thickness and slope analyses were performed.

608 ~~Deformation related to the shortest wavelength fold generation on thick breakout lava flows~~
 609 ~~is not continuous and occurs mainly in medial to distal zones. Subsequent multiple~~
 610 ~~generations of folds tend to span over the entire lava flows. Spectral analyses are mostly~~
 611 ~~homogeneous, with zones of high coherence mainly located on medial sectors (Fig. 6e). On~~
 612 ~~these thick lava flows, the second longest wavelengths (60–257 m, Table 2) as well as the~~

613 maximum dominant wavelengths (98–285 m, Table 2), continuously span the flow surface
 614 (Fig. 6e), and directly correlated with the virtually constant axial thickness observed in these
 615 lava flows (e.g., San Pedro N, Guallatiri, Licancabur S, Isluga, San Pedro NW; Fig. 6f;
 616 Supplementary material 2.4). Thin breakout lava flows show a folding pattern similar to their
 617 thicker counterparts. Multiple generations of folding and dominant wavelength also suggest
 618 a direct relation to lava thickness. The second-longest wavelength (40–80 m, Table 2) spans
 619 the flow surface intermittently (Fig. 7e), and the maximum dominant wavelengths (74–111
 620 m, Table 2) are generally discontinuous along the flow. Typically, on flows with thicker
 621 fronts, the maximum wavelength occurs in medial to distal areas, with spectral analyses
 622 showing continuous and homogeneous zones of high coherence (e.g., Paniri, Licancabur N,
 623 Licancabur M flows; Supplementary material 2.4).



624
 625 **Figure 7.** Diagram with the analyses performed on the Ollagüe S thin breakout flow. a) grayscale
 626 satellite image. b) thickness map. c) DEV map showing prominent ridges, frontal and lateral edges,
 627 and braided areas as high DEV values. e) bar plot of the dominant wavelengths. f) S-Transform

628 spectral analysis. h) thickness axial profile. The white line in the grayscale image represents the
629 profile along which the spectral, thickness and slope analyses were performed.

630 **4.5 Transitional flows**

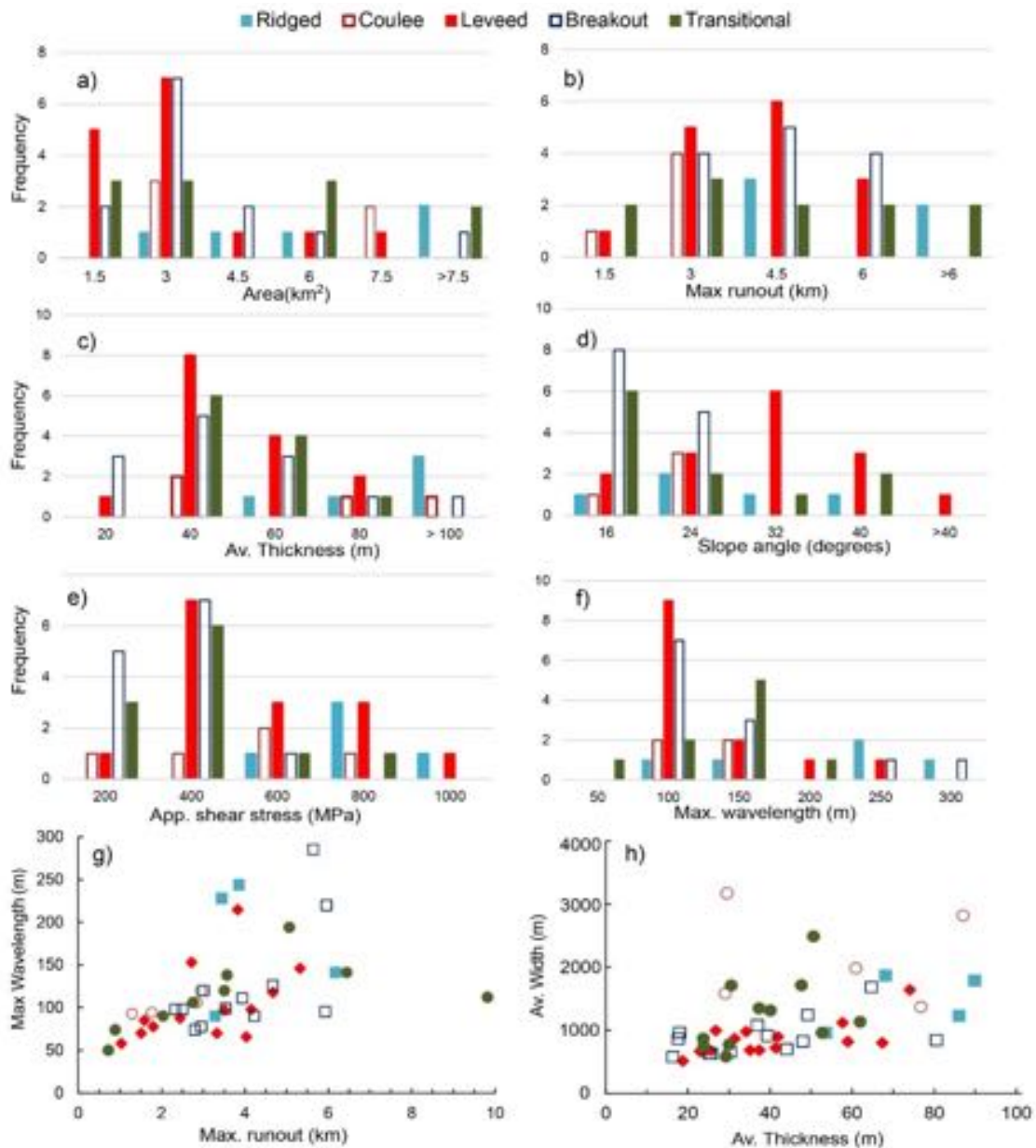
631 Several lava flows exhibit morphological features intermediate between the different types
632 (Fig. 2f, Supplementary material 1.5). This group includes lavas with variable morphologies,
633 less marked surface patterns, and/or variations in the plan view shape characteristics, making
634 it difficult to apply a univocal classification scheme.

635 Transitions between ridged and coulee lavas are recognized in two flows from the Falso
636 Azufre volcano (Falso Azufre E1 and Falso Azufre E2 flows, Fig. 2f, Supplementary material
637 2.5). Conversely, other lava flows also show characteristic features of leveed and breakout
638 lavas (Lullailaco S flow, or transitional between breakout and short leveed flows
639 (Sairecabur S flow). One small-volume flow from the Lastarria volcano (Lastarria SW flow)
640 suggests a transition between coulee and breakout flows (Supplementary material 2.5).

641 **4.6 General considerations on lava flow morphology**

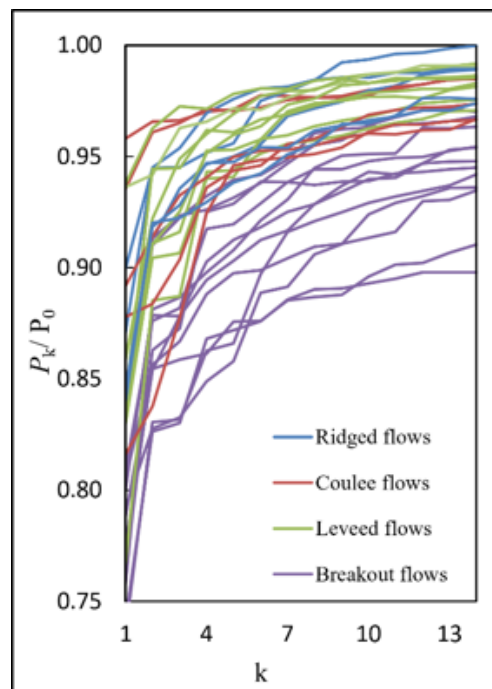
642 The variability of the morphological parameters typical of the different lava flows is well
643 illustrated in Figure 8, revealing for some of the flows a strict relation of the different types
644 of lavas with some of these parameters. Transitional and ridged flows are present at different
645 scales and are characterized by the largest variability of runout distance and invasion area
646 (generally between 1-10 km², except for the ridged Chao dacite flow, which covers an area
647 of about 60 km²). Conversely, breakout and leveed flows are mostly dispersed over areas <
648 3 km² and have maximum runouts between 3 and 6 km (Fig. 8a, b). The estimated **minimum**
649 **medium** thickness is always > 15 m in all the lava types; thickness is generally very high (up
650 to more than 100 m) in ridged flows, while leveed, breakout, and transitional flows have a
651 modal thickness between 20 and 40 m (Fig. 8c). Leveed flows are on average emplaced over
652 the steepest slopes (modal value of 32°) while coulee and breakout lavas are associated with
653 slopes always lower than 24° (Fig. 8d). Slope and thickness information are combined in the
654 calculated apparent shear stress responsible for the lava movement ($\tau_{app} = \rho \cdot g \cdot h \cdot \sin(\alpha)$,
655 where ρ is the lava density, g gravity acceleration, h thickness and α the slope angle). This
656 parameter can be considered a rough, first-order approximation of the maximum value for

657 the lava yield strength. More than half of the analyzed lava flows were emplaced under a τ_G
 658 lower than 400 MPa, with breakout flows having the lowest average values, while the highest
 659 τ_G values are associated with leveed and ridged lavas (Fig. 8e). Data on surface fold
 660 wavelength, although quite dispersed, show similar lower values for leveed and breakout
 661 flows (Fig. 8f), with the maximum wavelength positively correlated with the lava runout
 662 (Fig. 8g). Leveed and Breakout flows show more restricted widths than the other types,
 663 showing a linear relationship to thickness (Fig. 8h).



665 **Figure 8.** a to f) Frequency histograms of morphological and dynamical parameters
666 associated with the different types of lava flows; g) dependence of maximum wavelength of
667 surface ridges on maximum runout. h) relationship between average thickness and width for
668 the different types of lava flows (colors of symbols as for histograms).

669 Results of plain-view shape analysis clearly demonstrate that leveed lava flows have the less
670 complex morphologies, with P_k exceeding 0.95 for an average value of k of 4.1. Conversely,
671 breakout lavas show the more complex shapes (mainly due to lateral and frontal lobes), with
672 the lowest values of P_k that exceed 0.95 for an average k of 12.4. Ridged and coulee flows
673 exhibit shapes with intermediate complexities (Fig. 9), as well as transitional flows (not
674 shown) (Fig. 9).



675

676 **Figure 9.** Plot of k values vs P_k/P_0 . Initial low values of P_k/P_0 and steep slopes correspond to plain-
677 view complex morphologies, while relatively gentle initial slopes that rapidly flatten indicate simple
678 shapes. Transitional flows are not included to avoid overlapping.

679 5. Discussion

680 5.1 Effect of apparent viscosity

681 The mechanisms of lava flow folding and the resulting fold wavelengths have been largely
682 discussed in terms of their relations with compressive stress, thickness of the folded layer,

683 vertical and horizontal gradients of temperature, lava viscosity and density (Fink and
684 Fletcher, 1978; Fink, 1980; Lescinsky et al., 2007; Favalli et al., 2018). The maximum
685 dominant wavelength has been used to constrain the thickness and viscosity of the folded
686 layer and the compressive stress (Fink and Fletcher, 1978; Gregg et al., 1998; Castro and
687 Cashman, 1999; Cashman et al., 2013; Deardorff et al., 2019). However, results from our
688 morphological analysis show that the maximum wavelength of surface folds largely varies
689 between the different lava types, with a correlation with lava runout and, to a lower extent,
690 lava thickness.

691 A general relation links maximum wavelengths of folds and SiO₂ content, with basaltic flows
692 characterized by small folds and wrinkles (generally < 2 m in plain-view) while many
693 evolved lavas present large, mesoscopic-scale ridge and through structures commonly
694 interpreted as folds (Fink, 1980; Gregg et al., 1998; Cioni and Funedda, 2005; Deardorff et
695 al., 2019). However, in the andesite-to-dacite range investigated in this study, the comparison
696 between the maximum dominant wavelength, ~~computed using the S transform method~~, and
697 composition does not show a statistically significant correlation (Fig. 10a). This is consistent
698 with previous data (Gregg et al., 1998; Pylle and Elliot, 2006; Lescinsky et al., 2007;
699 Deardorff et al., 2019) and with the observed wide spectrum of lava morphologies within the
700 restricted SiO₂ range considered here. This also translates into a poor correlation of maximum
701 wavelength with lava viscosity (Fig. 10c). In fact, although the dataset spans a relatively
702 restricted range of SiO₂, viscosities calculated for some selected flows (for which data on
703 crystal content and bulk rock compositions are available) largely varies with SiO₂ (and
704 corresponding crystal content) of the melt (Fig. 10b). Viscosity modeling returns a range of
705 values that spans over 6 orders of magnitude (Table 4). Crystals are able to increase the melt
706 viscosity by up to more than 5 orders of magnitude (Costa et al., 2009; Chevrel et al., 2013;
707 Table 4; Fig. 10b), with the maximum values associated with coulee and ridged lavas (~10¹⁰
708 – 10¹¹ Pas; Table 4, Fig. 10b). However, the effect of crystals cannot be simply modeled by
709 assuming a monodispersed population (Cimarelli et al., 2011) because the maximum packing
710 fraction increases with polymodality (Klein et al., 2017). Thus, phenocrysts and microlites
711 do not have the same rheological effect. The presence of crystals also enhances the non-
712 Newtonian behavior of lava flows, inducing shear thinning and viscoelastic effects (Caricchi
713 et al., 2007; Castruccio et al., 2010; Mueller et al., 2011; Klein et al., 2017; Giordano, 2019).

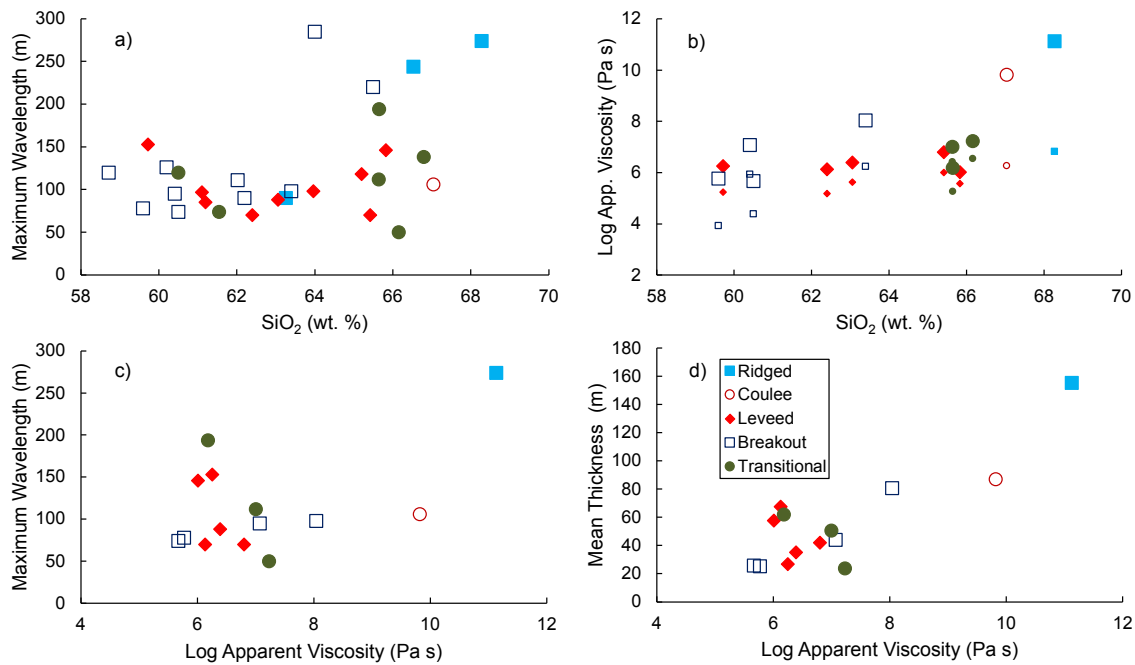
714 In general, the CVZ lava flows present a high-crystal content with rheology clearly
715 approaching a non-Newtonian behavior (as testified, for example, by the formation of coulee
716 or leveed lava flows). Calculated yield strengths vary in the range $\sim 10^4$ - 10^6 Pa (Hulme, 1974;
717 Moore et al., 1978), suggesting that the flow advance could also be controlled by the onset
718 of a core yield strength (Castruccio et al., 2013). While the value of the yield strength is not
719 clearly correlated to any morphological parameter of the investigated lava flows, calculated
720 viscosity shows a good positive correlation with the average lava flow thickness (Fig. 10d).
721 This suggests that the effective viscosity may represent a first-order factor controlling the
722 general thickness, and possibly, the runout of the lava flow.

723 **Table 4.** Melt, relative, and apparent viscosities for the CVZ lava flows with available composition
724 and crystallinity. n_{melt} : liquid viscosity, n_r : relative viscosity, n_{app} : apparent viscosity

Flow	Type	Log(n_{melt}) Pa s	Log(n_r) Pa s	Log(n_{app}) Pa s
Chao dacite	Ridged	6.82	4.31	11.13
Chac-Inca W	Coulee	6.26	3.56	9.82
Irruputuncu U	Leveed	5.18	0.95	6.13
Irruputuncu L	Leveed	5.24	1.01	6.25
Llullaillaco U	Leveed	6.00	0.80	6.80
Llullaillaco N	Leveed	5.57	0.44	6.01
Olca-Paruma M	Leveed	5.62	0.77	6.39
Lastarria N	Breakout	5.93	1.14	7.07
Licancabur N	Breakout	4.38	1.29	5.67
Licancabur M	Breakout	3.93	1.84	5.77
Guallatiri	Breakout	6.24	1.80	8.04
Uturuncu	Transitional	6.42	0.58	7.00
Llullaillaco S	Transitional	5.26	0.92	6.18
Lastarria SW	Transitional	6.55	0.68	7.23

725 Overall, thin, breakout lava flows (e.g., Licancabur volcano flows) present the lowest
726 viscosities, with values of the order of 10^5 Pa s, while the thicker flows of the same category
727 are crystal-richer and have viscosities 2-3 orders of magnitude higher (Table 4). The viscosity
728 of channelized leveed lavas does not present significant differences between long and short
729 flows, with values of about $\sim 10^6$ Pas. Coulee lavas are high-viscosity flows, with values of
730 up to 10^{10} Pas, which is consistent with their morphological and emplacement characteristics
731 similar to lava domes (Watts et al., 2002; Lescinsky et al., 2007). We obtained the highest
732 apparent viscosity for the Chao dacite (ridged lava flow) , which derives from the

733 combination of its crystal-rich nature ($\phi_f > 0.3$) and high SiO₂ content. As expected,
 734 transitional flows exhibit an intermediate behavior.

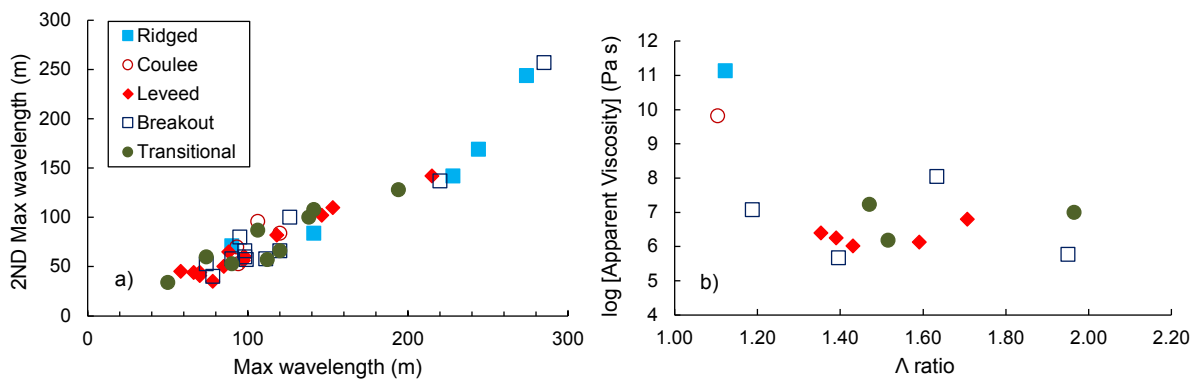


735
 736 **Figure 10.** a) Composition vs. maximum wavelength shows a poor correlation, with significant
 737 overlapping between the different lava groups, especially in the range 64-67 SiO₂ wt.%. b) Large
 738 symbols represent the calculated apparent viscosity of the lava, while small symbols indicate only the
 739 viscosity of the residual melt (n_{melt}). The effect of crystals induces a sharp increase in the apparent
 740 viscosity (up to 5 orders of magnitude). Note that flows with higher SiO₂ contents may present lower
 741 apparent viscosity than more crystalline and less evolved lavas. c) Apparent viscosity vs. maximum
 742 wavelength shows a poor correlation. Despite the broader range of viscosities for breakout flows
 743 compared to leveed flows, they present more restricted maximum wavelengths, suggesting that the
 744 maximum wavelengths in leveed flows may be strongly ruled by other parameters such as effusion
 745 rate. d) Plot of the apparent viscosity vs. the mean thickness shows a positive correlation, suggesting
 746 that the dynamics of ridged and coulee flows, and to a lesser extent of thick breakout flows, may be
 747 strongly controlled by their high viscosities.

748 5.2 Other parameters controlling the morphology of the lava flows

749 The observed relation between maximum surface fold wavelength and runout (Fig. 8g)
 750 clearly indicates the role of progressive deformation (and strain accumulation) in the build-
 751 up of these structures. The ratio Λ between the maximum wavelength and the second-

752 maximum wavelength has been related to the relative rates of cooling at the flow surface and
 753 shortening by compression (Gregg et al., 1998), especially in the case of lava crust formation.
 754 This ratio varies between the different types of lava flows (Fig. 11a), with strictly similar
 755 average values for ridged flows and coulee lavas (1.42 ± 0.23 and 1.41 ± 0.28 , respectively)
 756 and slightly different, higher values for the other three types (1.58 ± 0.24 for leveed flows,
 757 1.55 ± 0.28 for breakout flows and 1.51 ± 0.26 for transitional flows). Although these values
 758 are slightly lower than reported data (2.1 ± 0.3 for dacite lavas; 1.8 ± 0.4 for rhyolite lavas;
 759 Gregg et al., 1998), our results are quite consistent with previous studies that attempted to
 760 link Λ with composition (Gregg et al., 1998; Pyle and Elliot, 2006; Hunt et al., 2019; Farrell
 761 et al., 2018; Deardorff et al., 2019). The lava flows with the lowest values of Λ (ridged flows
 762 and coulee lavas; Λ close to 1.1 in Fig. 11b) are, in fact, associated with the largest apparent
 763 viscosity values and, hence, strain rates (Fig. 11b), while all the other lava flows have similar
 764 viscosities, nearly 3 orders of magnitude lower than the others (Fig. 11b). The low strain rates
 765 retard fold formation so that the difference between the two larger fold wavelengths is
 766 reduced.

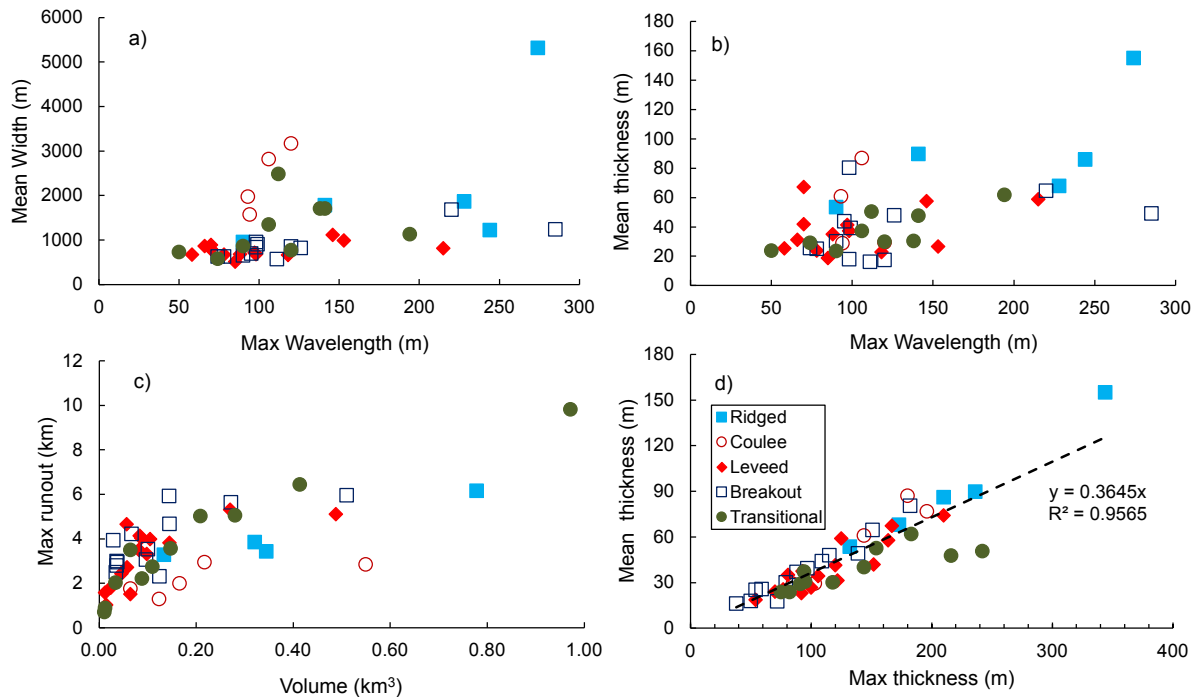


767
 768 **Figure 11.** a) Maximum wavelength vs. the second maximum wavelength. A linear relationship is
 769 observed between wavelengths in the range 50-250 m. b) Λ vs. apparent viscosity. Two main groups
 770 are identified: one group with variable Λ values and viscosities in the range 10^6 - 10^7 Pa s⁻¹, and the
 771 other with small Λ and n_{app} that exceed 10^8 Pa s⁻¹.

772 Thickness and fold wavelengths, and their spatial distribution, can record the characteristics
 773 of the flow dynamics during emplacement. According to the different models of folding
 774 adopted (Biot, 1961 Fink and Fletcher, 1978; Castro and Cashman, 1999), the maximum
 775 dominant wavelength increases as a function of the thickness of the flow or of the rigid upper
 776 part of the lava flow (Fig. 12b). For example, Fink (1980) described fold formation in

777 rhyolitic lava flows as related to the progressive growth of a rigid crust, in analogy with
778 basaltic lavas (Fink and Fletcher, 1978; Farrell et al., 2018). Conversely, Cioni and Funedda
779 (2005) described folds in crystal-rich comenditic lavas of Sardinia (Italy) as related to a
780 process similar to the buckling of the entire thickness (more than 20 m) of the lava flow. In
781 general, the lava thickness and the maximum dominant wavelength are not homogeneous
782 along the surface of the flow, with maximum wavelength depending on the local thickness
783 distribution and the flow type (Figs. 3-7). Overall, the highest values of thickness and
784 wavelength occur in the central channel of ridged flows more than 100 meters thick. In coulee
785 flows, the maximum thickness occurs close to the vent area and is not directly related to the
786 maximum wavelength distribution. Leveed flows show a unique downflow toe of maximum
787 thickness and wavelength. Long leveed flows show longer maximum wavelengths than short
788 flows, and the maximum wavelength for this type of flows shows a regular variation with
789 their mean width (Fig. 12a). Similarly, breakout flows show a direct relation between
790 maximum wavelength and mean flow width (Fig. 12a). In general, thin breakout flows have
791 the lowest maximum wavelengths (Fig. 12b), while thicker breakout flows display higher
792 maximum wavelengths typically developed more homogeneously and continuously along the
793 central channel.

794 However, it is clear from our data that thickness alone does not fully control the folding
795 pattern and that other factors (like flow width, runout or viscosity) can play a significant role
796 in the resulting deformation pattern. In fact, thickness and runout are also governed by
797 viscosity (Castro and Cashman, 1999; Griffiths, 2000; Castruccio et al., 2013), and thus both
798 these parameters clearly control maximum wavelength formation (Fig. 10d). The dependence
799 of maximum wavelength with lava runout (Fig. 8f) has already been discussed in terms of
800 fold growth by progressive deformation during flow.



801

802 **Figure 12.** a) Maximum width vs. mean wavelength. Coulee flows do not show a good correlation, suggesting that other parameters, such as thickness, may control the maximum wavelength. On the other hand, Leveed flows show a good correlation between maximum wavelength and mean width. b) The maximum wavelength increase as a function of the flow thickness. Ridged flows have the highest values suggesting a strong control of thickness in folding. c) Volume vs. maximum runout shows a positive correlation as the final volume depends on the eruption time and the effusion rate (that partially controls the runout). Larger flows reach longer distances; however, the overlap is significant at low volumes, with coulee flows showing the lowest runout at a given volume d) maximum thickness vs. mean thickness shows a very good positive correlation with mean thickness/Max thickness similar to 0.3645.

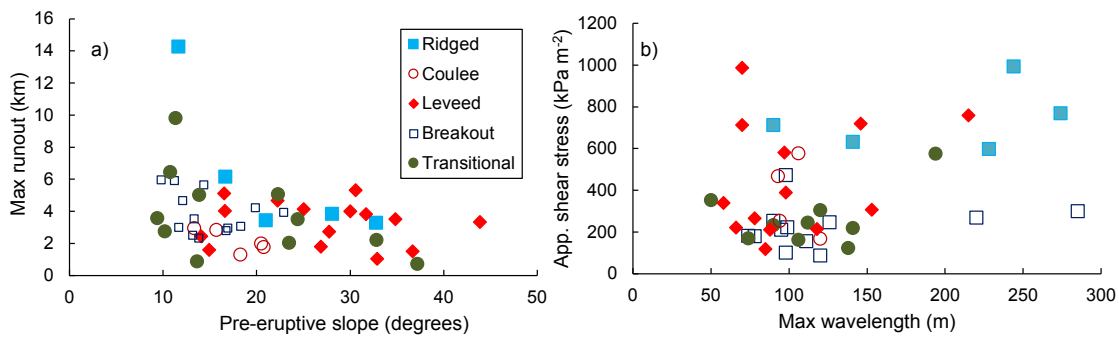
812 Volume and runout of lava flows are quite closely related (Fig. 12c), with larger flows reaching the maximum distances. The four lava flow types here defined depict good trends between these two parameters, with breakout flows typically associated with larger runouts, and coulees with smaller runouts, for a given flow volume. Ridged flows have on average large runouts and the largest volumes (with up to more than 9 km of runout and 10 km³ of volume for the Chao dacite, not shown in Fig. 12c). The Cerro Uturuncu lava flow, classified as transitional due to the presence of a ridged surface and marginal levees and a lateral lobe, reaches a runout of near 10 km, plotting on the same trend of ridged lavas.

820 The maximum thickness observed for the different lava flows is strictly related to the mean
821 thickness (calculated as the ratio between the calculated volume and measured area of the
822 lava flow). Therefore, we suggest using the very good correlation between these two values
823 (Mean thickness/Max thickness = 0.3645; Fig. 12d) for a first-order calculation of lava flow
824 volumes from measurements of the lava flow area and observed estimated maximum
825 thickness.

826 **5.3 The role of the pre-eruptive surface slope**

827 The pre-eruptive slope is one of the most important control parameters for maximum runout
828 of mafic lava flows (Walker, 1967; Hulme, 1974), together with other important factors such
829 as viscosity and effusion rate (Walker, 1973). Conversely, the intermediate to silicic lava
830 flows studied here show a very weak dependence of runout with the slope, with significant
831 scattering for all the lava types, suggesting a dominant effect of other parameters (Fig. 13a).
832 In general, for a given effusion rate and initial viscosity, lava flows emplaced on steeper
833 slopes are longer and faster. However, it is crucial to consider the flow type when interpreting
834 flow length (Walker, 1973; Gregg and Fink, 2000; Harris and Rowland, 2009). Branching,
835 and consequently lava flow morphology, are partially controlled by the slope as it impacts
836 the thickness, width, and flow advance rate (Dietterich and Cashman, 2014). In the CVZ,
837 branching is a distinctive feature only appreciated at a scale of flow segments in medial and
838 distal areas of breakout flows over a low slope. Typically, the slope exerts an important
839 control on flow thickness, such that lava flows thicken on low slopes and thin on steep slopes
840 (Lister, 1992; Griffiths, 2000; Gregg and Fink, 2000; Dietterich et al., 2015). However,
841 considerable overlapping occurs in thickness values in flows emplaced on 10-25° surfaces
842 (Table 2), suggesting that thickness is mainly controlled by other factors (e.g., viscosity,
843 mode of deformation) with reciprocal, not linear, relationships.

844



845

846 **Figure 13.** a) Pre-eruptive surface slope vs. maximum runout. This plot shows significant overlapping
 847 between the different lava types, suggesting that the pre-eruptive topography by itself may only exert
 848 a minor control in the runout distance of the CVZ lavas. b) Maximum wavelengths vs. apparent shear
 849 stress. This plot suggests that a combination of thickness and slope may control the folding process.
 850 Coulee lavas have a more restricted range of dominant wavelengths with variable τ_G , and ridged and
 851 breakout lavas have broad ranges of dominant wavelengths, despite presenting high and low τ_G
 852 values, respectively.

853 On the other hand, data from Table 2 suggest a significant effect of average slope in
 854 controlling the maximum thickness of the flow. The maximum thickness of leveed lava flows
 855 tends to increase with slope, while thickness of ridged lavas shows an inverse correlation.
 856 Conversely, the maximum thickness of coulee and breakout lava flows appears nearly
 857 independent from the slope. We suggest that these very different behaviours derive from the
 858 combined effect of lava viscosity and effusion dynamics (see section 5.5).

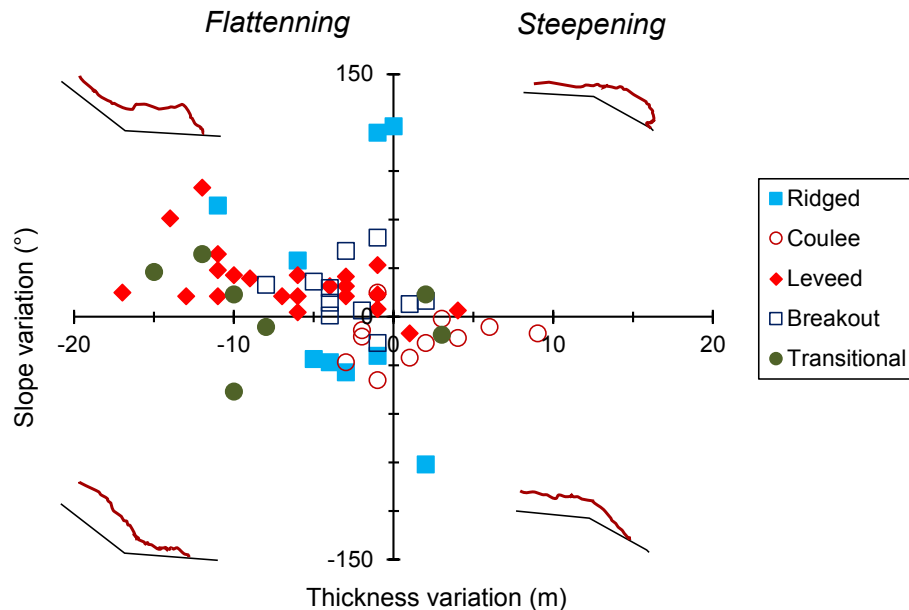
859 Regarding lava width, this parameter may be primarily controlled by the characteristics of
 860 the underlying surface (Hulme 1974; Lister, 1992; Kerr et al. 2006; Dietterich and Cashman,
 861 2014; Richardson and Karlstrom, 2019). Flows are narrower on steeper slopes, generally
 862 enlarging into wider, fan-shaped zones on distal areas. Flow width is determined by the
 863 competition between cross-slope flow spreading and lava cooling or crust formation
 864 (Cashman et al., 2013). The larger widths are observed in ridged and coulees flows or in
 865 some transitional lava flows, while minimum values occur in strongly channeled leveed and
 866 thin breakout flows (Figs. 8h, 12a).

867 As a matter of fact, the control of viscosity and, to a variable extent, of pre-eruptive slope
 868 on thickness, together with effusion rate, govern the dynamics of the flow, affecting flow

869 velocity and directly impacting different morphological features such as runout, width, and
870 general deformation dynamics. This is ~~clearly demonstrated~~ suggested by the roughly
871 positive ~~quite strong~~ relationship existing between the maximum wavelength of flow
872 deformation and the gravitational component of the shear stress τ_G applied to the lava flow
873 (Fig. 13b). This suggests that thickness and slope, and hence other related parameters such
874 as emplacement velocity, may partially control the folding process. For example, the
875 presence of breaks in the slope of the underlying surfaces may control the distribution and
876 continuity of the different wavelengths along the flow path, as the spectral analysis shows a
877 positive correlation between changes in the pre-eruptive surface and the influence area of
878 minor wavelengths (see Supplementary material 2).

879 **5.4 Effects of breaks in slope**

880 The occurrence of breaks in slope at a local scale, depending on the local slope and the flow
881 rate, may impact lava flow width, thickness, and branching (Dietterich and Cashman, 2014;
882 Harris and Rowland, 2015). The different types of lava flows present a systematic correlation
883 between lava thickness upstream or downstream from a break in slope, while no clear
884 relationship between thickness and steepness of the break in slope is recognized. . In general,
885 the lava flows adjust thickness to the new slope after a break in slope. Most flows thicken as
886 slope flattens; ridged flows have the largest thickness increase even with small changes in
887 the slope, although some flows (e.g., Acotango, Chao dacite, and Ollagüe NW) present a
888 thickness decrease after the slope flattening (Fig. 14). Only a few lava flows develop slightly
889 thicker zones as they pass to steeper slopes (Fig. 14). Additionally, coulee lavas show a
890 general decrease in thickness with distance, independent of the slope break. The thickness
891 decrease with slope flattening observed for ridged and coulee lavas suggests a prominent role
892 of viscosity increase with distance, which slows down (or stops) the increase in thickness of
893 the lava front.



894

895 **Figure 14.** Diagram of thickness variation concerning breaks in slope. The upper left and lower right
 896 areas correspond to the expected behavior of thickness to changes in the underlying slope, while the
 897 other areas represent zones of inheritance (they have unexpected thickness variations as they decrease
 898 in thickness on more flattening surfaces and vice versa). All coulee flows decrease in thickness
 899 independent of the slope, while leveed flows show the expected behavior in response to variations in
 900 the slope, typically increasing in thickness to downslope. Some ridged flows suggest inheritance as
 901 they decrease in thickness as they flatten. Breakout flows do not show significant inheritance.

902 Conversely, the very large thickening (up to more than 100 m; Fig. 14) of some ridged flows
 903 suggests a long-lasting high mobility of the lava possibly related to high effusion rates.
 904 Leveed lavas are characterized by a nearly ubiquitous increase in thickness with a flattening
 905 slope, suggesting continued flow mobility after levee formation, so resulting in the partial
 906 drainage of the channel (Borgia and Linneman, 1990; Naranjo et al., 1992; Harris and
 907 Rowland, 2009; Cashman et al., 2013). Similarly to basaltic lavas, the development of the
 908 channel could, in fact, result in a general velocity increase to comply mass conservation,
 909 which possibly explains the generally large runout of these flows despite their small volume
 910 (Hulme, 1974; Pinkerton and Wilson, 1994; Glaze et al., 2009) (Fig. 12c). Breakout flows
 911 do not show significant thickness variations with slope changes. The small thickness increase
 912 (about 10 m) with steepening shown by some flows is possibly comprised within the error in
 913 thickness estimation (derived from the difference between the present topography and the
 914 reconstructed basal surface of the lava). The general effect of breaks in the slope of the basal

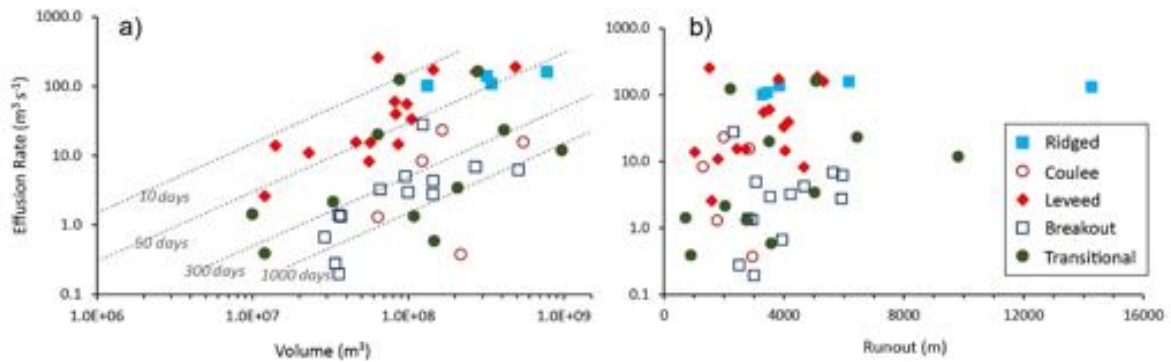
915 surface seems to result only in thickness changes at the local scale, without determining
916 downflow changes in the other characteristics of the lava flow. Lev et al. (2019) performed
917 experimental analyses and investigated the direct effect of the slope breaks on the flow
918 velocity. They demonstrated no predictable inheritance of channel width with a steepening
919 or shallowing of the underlying bed, with only a direct relationship between slope and flow
920 velocity.

921 **5.5 Eruption conditions**

922 ~~The proposed classification~~ This proposed differentiation of lava flow types, mainly based
923 on their surface morphology and shape characteristics, produces significantly overlapped
924 groups when other descriptive parameters are considered (Fig. 8). This may be attributed to
925 our limited knowledge of the emplacement conditions for flows of intermediate to silica-rich
926 compositions (Deardorff and Cashman, 2012; Tuffen et al., 2013; Deardorff et al., 2019) due
927 to their infrequent occurrence and only sparse (or absent) real-time observations.
928 Observations are mainly limited to andesitic leveed lava flows (Borgia et al., 1983; Naranjo
929 et al., 1992; Navarro-Ochoa et al., 2002; Harris et al., 2003; Wadge et al., 2014). Although
930 rhyolitic, the well-described 2011 lava of Cordon Caulle (Chile; Tuffen et al., 2013;
931 Farquharson et al., 2015) can be classified as a breakout/ridged flow. For this reason, source
932 parameters controlling the emplacement of silicic lava flows are poorly constrained by direct
933 observations, and analysis of morphological and rheological features of past lava flows
934 remains the only method to define at least the range of their variability. Numerical models
935 for estimating parameters such as the effusion, cooling, and crust growth rates often require
936 several assumptions that may increase the uncertainty. In particular, several methods have
937 been proposed for estimating effusion rates and other rheological parameters of basaltic lavas
938 from their observation (among others, Jeffrey, 1925; Pinkerton and Sparks, 1976; Kerr et
939 al., 2006; Harris et al., 2007; Harris and Rowland, 2009). In addition, the results of these
940 calculations are often typically underestimated, resulting in average values which do not
941 consider the temporal fluctuations or variations of these parameters (Naranjo et al., 1992;
942 Navarro- Ochoa et al., 2002; Pallister et al., 2013; Bertin et al., 2015).

943 Using an experimental approach, Lyman et al. (2004) proposed that equation (1) reported at
944 section 2.2 could be used to predict effusion rates Q_e of silicic lava flows and domes starting

945 from their morphological features. Under the approximation of σ_0 as derived from lava
 946 morphology, we calculated the theoretical Q_e of all the studied lava flows (Table 2 and Fig.
 947 15a).



948
 949 **Figure. 15** a) Volume of the different lava flows vs. effusion rate. Hatched lines are
 950 isochrones. b) Runout of the different lava flows vs. effusion rate. Different lava flows show
 951 a poor correlation.

952 Effusion rate well correlates with lava volume for the different types of lava (Fig. 15a) and,
 953 unexpectedly, only to a lower extent with runout distance (Fig. 15b). Larger volume lavas
 954 generally correspond to higher Q_e , with leveed and ridged lavas being emplaced more rapidly
 955 (over times of a few days) than the other lava flows. Ridged lavas also present high, poorly
 956 variable effusion rates, with Q_e generally larger than $100 \text{ m}^3\text{s}^{-1}$. Effusion rates of breakout
 957 lavas and coulees are lower and span over about 2 orders of magnitudes, which translates
 958 into effusion durations between months and a few years (Fig. 15a).

959 Ridged and coulee flows have different characteristics that are possibly modulated both by
 960 the effects of largely different effusion rates (Fig. 15a) and similar rheology. Coulee flows
 961 have transitional features between high-viscosity lava flows and domes. They resemble the
 962 lobate to platy morphologies obtained experimentally by Fink and Griffiths (1998) and
 963 Lyman et al. (2004), which derive from low eruption rates. Coulee lavas are emplaced on
 964 gentle to medium slopes with initially radial growing due to inflation of the solidified crust
 965 (Griffiths and Fink, 1997), while as the volume increases, the gravitational forces become
 966 significant, inhibiting a general thickening and starting to spread the flow laterally (Lescinsky

967 et al., 2007). Flow emplacement possibly occurs over a long period, of the order of up to
968 several years.

969 Elongated ridged flows may be emplaced with higher effusion rates and underlying slopes
970 (de Silva et al., 1994) than coulees. While for basaltic lavas, thermal insulation is efficiently
971 produced by the formation of a thick crust (Harris et al., 2002; Bullock et al., 2018), the high
972 flow rate of these highly viscous flows contributes to rapidly increases their thickness, so
973 minimizing heat losses. As a result, the flow may advance further (Fig. 12c) before cooling
974 becomes a substantial factor forcing stagnation (Fink and Griffiths, 1998; Harris et al., 2002;
975 Magnall et al., 2017).

976 Leveed flows have a channeled nature, which, together with steep initial slopes ($> 30^\circ$),
977 strictly agrees with the calculated high effusion rates (Walker, 1973; Fink and Griffiths, 1990;
978 Gregg and Fink, 2000; Harris and Rowland, 2009) and the low, restricted values of viscosity
979 (Fig. 10, Table 4). The advance rate of these flows and the gradient between steep proximal
980 zones and more flat toes may induce high stress to the surface crust flow (Kilburn, 2004;
981 Magnall et al., 2017), triggering a more regular disruption as testified by the rough surface
982 with small blocks (Legget et al., 2020). The generally low volume fraction of microlites of
983 this type of lavas suggest rapid magma ascent, extrusion, and emplacement (Cashman and
984 Blundy, 2000; Watts et al., 2002). These flows strictly resemble the levee flows
985 experimentally obtained by Gregg and Fink (2000), who clearly demonstrated that they are
986 formed under conditions of low cooling (made easier by the generally high thickness; Fig.
987 15b) and high effusion rates.

988 Breakouts and overflows typically of breakout flows (and some transitional flows) arise when
989 the flow halts and the lava is continuously supplied, resulting in inflation and increased
990 internal pressure (Calvari and Pinkerton, 1998). As the pressure exceeds the local confining
991 force, a rupture of the surface crust or the levees occurs, redirecting the flow and forming
992 new lobes (Pinkerton and Sparks, 1976; Farquharson et al., 2015; Magnall et al., 2018). This
993 process may cause lower thicknesses of thin breakout lavas, as it can divide the lava flux into
994 multiple branches reducing the flow thickness and the flow advance rate (Lister, 1992;
995 Dietterich and Cashman, 2014; Magnall et al., 2018). Breakouts can be formed due to
996 oscillations in the effusion rate, which propagate an increased supply of lava to the flow front

997 or along the flow margins (Dietterich et al., 2012; Magnall et al., 2017). These processes
998 have been well described for the 2011-2012 Cordon Caulle eruption, where the morphology
999 changed from a simple to compound flow with lateral lobes 64-116 days after the eruption
1000 started. This morphology change occurred during a phase of general decrease of the effusion
1001 rate (10-20 m³s⁻¹; Bertin et al., 2013) that followed the initial phase of effusion rate (50-70
1002 m³s⁻¹; Bertin et al., 2013), reflecting a progressive stagnation of the flow fronts and margins
1003 (Tuffen et al., 2013). As demonstrated by the Cordon Caulle lava, emplacement of breakout
1004 flows can occur over long periods, which supports the average low effusion rates calculated
1005 for this lavas in the CAVZ (Fig. 15a).

1006 ~~Lavas with morphological features transitional between leveed and breakout flows are~~
1007 ~~common, suggesting that they may be due, at a first order, to large effusion rate fluctuations,~~
1008 ~~as well as to the influence of all the other important parameters discussed in the text~~
1009 ~~(rheology, pre-existing topography).~~

1010 **5.6 Morphology-based characterization of intermediate blocky lavas**

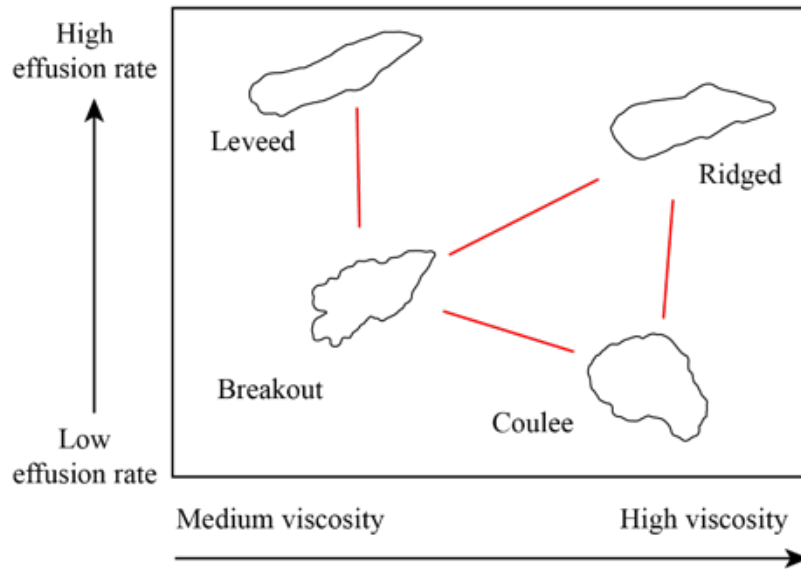
1011 The efforts to define and classify the morphology of the different lava flows are typically
1012 based on descriptive terms related to their surfaces or the to presence of peculiar features
1013 (slabs, ropes, etc.). Finch (1933) introduced the word “Block lava” as a merely descriptive
1014 term for lava flows mainly formed by dense blocks and markedly different from the scoria-
1015 covered surface of a‘ā lavas or the smooth surface of pahoehoe lavas This tripartite
1016 descriptive classification was rapidly expanded, including subgroups mainly derived from a
1017 complete intergradation between pahoehoe and a‘ā lavas, with particular characteristics
1018 typically belonging to both groups (Jones, 1943; Macdonald, 1953; Wentworth and
1019 Macdonald, 1953). However, these subtypes are generally defined qualitatively and are
1020 typically based on the morphology of the flow interiors, including the presence, size, shape,
1021 and distribution of vesicles, as well as the presence and type of shear structures (Harris et al.,
1022 2016), being univocal and in some cases subjective.

1023 Jones (1943) attempted to qualitatively classify the lava flows as a function of their surfaces
1024 from smooth to rough and structurally from solid (or massive) to weak (Table 1 from Jones
1025 1943). Although the classification only includes subgroups for mafic lavas, it recognized (but

1026 did not include) the need for divisions for blocky lavas. Harris et al. (2016) deeply reviewed
1027 and presented a descriptive scheme to classify the different lavas. Again, this classification
1028 was mainly focused on pahoehoe and a'ā flows, classifying silicic flows as block lavas and
1029 subdividing them into blocky or rubbly mainly based on their breccias.

1030 We performed a systematic morphological and morphometrical characterization of
1031 intermediate to silicic lava flows, evidencing four main types. This division is based on
1032 descriptive elements including the presence of particular features such as lobes, levees or
1033 types of ridges, the shape of the flow and a set of morphometrical data. A correct
1034 characterization with a consistent application of these proposed types may allow us to link
1035 the different flows of similar characteristics with their common dynamics and emplacement
1036 mechanisms. Lava flows with characteristics related to more than one group are also
1037 considered here and generically defined as Transitional lavas. As for pahoehoe to blocky
1038 lavas, intersections between the different morphologies are common and may be related to
1039 fluctuations of the complex eruptive dynamics during lava flow emplacement.

1040 As we discussed in the previous sections, the morphology of these lavas is not controlled by
1041 a single parameter, being generally the result of the combined effects of the topography,
1042 rheological properties of the magma, and effusion rate. We categorized in a schematic
1043 illustration (Fig. 16) the different types of lavas here identified as a function of the η_{app} and
1044 the effusion rate, although we demonstrated also a clear role of topography and pre-eruptive
1045 surface slope.



1046

1047 **Figure 16.** Qualitative scheme for the division of the identified lava flow types. Red lines
 1048 represent transitions between the different types.

1049

6. Summary and conclusions

1050

1051

1052

1053

1054

1055

1056

1057

1058

1059

The advance rate of intermediate to silicic lava flows and their morphologies result from the combined effect of topography, effusion rate, and the progressively changing lava flow rheology, governed by composition, crystallization, cooling, and crustal growth rates (Farquharson et al., 2015). Moreover, the surface morphology of the lava flows, and especially the shape and wavelength of surface deformations, have been largely discussed both as the result of rigid behavior forming faulted ogives or as the result of a complex folding process. The generally large value of the dominant wavelength of the surface deformations, comparable in many cases to the mean thickness of the lava flow, suggests that deformation involves a large portion of the lava flow, and it is possibly controlled also by the width of the lava itself.

1060

1061

1062

1063

1064

1065

of the plain-view shape, thickness, surface texture and pre-eruptive topography contribute to better define the field of existence of the different lava types. The FD analysis of the plain-view shape of the flows and the S-transform method based on grayscale images to describe surface textures are two powerful tools to remotely characterize these lava flows, even without availability of high-resolution DEMs. In general, thickness and the maximum dominant wavelength of the folding pattern are not homogeneous along the surface of the

1066 flow, with the maximum wavelength spatially related to the local thickness and the flow type.
1067 In addition, the maximum dominant wavelength is poorly correlated with SiO₂ content and
1068 partially with lava viscosity. Therefore, the control of pre-eruptive topography and viscosity
1069 (with variations of several orders of magnitude) on thickness, together with effusion rate,
1070 may govern the general dynamics of the flow, directly impacting the different morphological
1071 features. This is supported by the **positive** ~~quite strong~~ relationship between the surface
1072 maximum wavelength and the gravitational component of the shear stress applied to the lava
1073 flow (Fig. 13b).

1074 Mainly based on morphology analysis from remote data, four different types of andesitic to
1075 silicic lava flows are distinguished (Fig. 17), together with an additional transitional group:

1076 a) Ridged lavas have highly arcuate ridges with convex surfaces, large thicknesses, long
1077 maximum wavelengths, and one rounded frontal lobe. They are high-volume and
1078 crystal-rich, and are emplaced under high effusion rates on variably sloping
1079 underlying surfaces. The wavelength of deformation, comparable to the thickness,
1080 suggests a folding process involving nearly the entire lava flow. They are possibly
1081 associated with short-lasting eruptions.

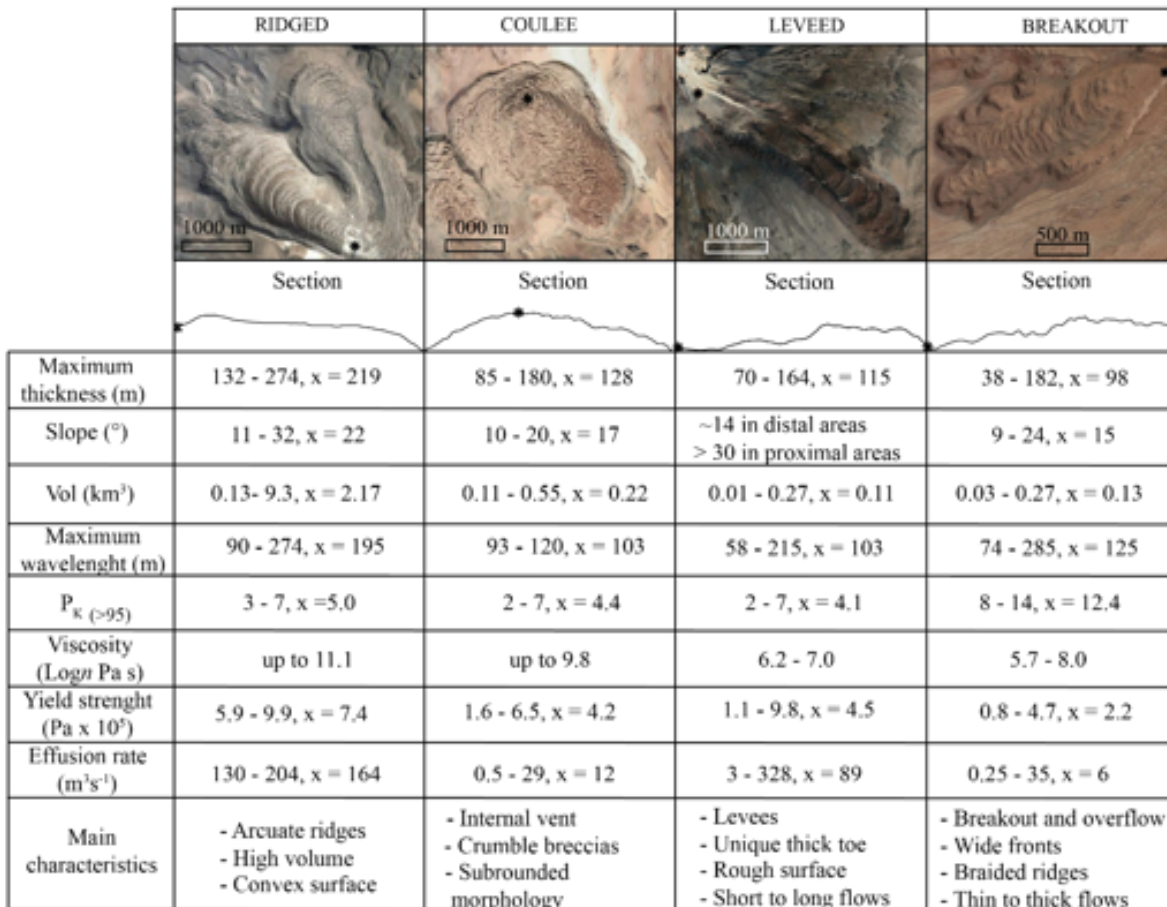
1082 b) Coulee lavas have characteristics between high-viscosity lava flows and domes. They
1083 have relatively simple shapes with lengths that do not significantly exceed their
1084 widths. Their vents are located inside the flow, and large ridges and crumble breccias
1085 span the surface. They are emplaced on gentle to medium slopes, with initial radial
1086 growth due to inflation of the solidified crust (Griffiths and Fink, 1997). The generally
1087 large thickness and the maximum deformation wavelength, only a few times the mean
1088 thickness and far smaller than the mean lava width, suggest that deformation was
1089 mainly dependent on thickness, without an important role of the lateral dimensions
1090 of the flow. This implies that only the internal resistance to the flow (viscosity, yield
1091 strength), and possibly the effusion rate, controlled deformation. ~~Effusion rates are~~
1092 ~~generally low, and~~ Effusion may prolong for months to years

1093 c) Leveed lavas have the simplest shapes and are highly channelized with a unique
1094 frontal toe, generally of maximum thickness. ~~They have restricted viscosities and~~
1095 ~~often occur over high initial slopes (> 30°).~~ The **ir** channelled nature and steep initial

1096 slopes indicate high effusion and advance rates (Gregg and Fink, 2000); while ~~In~~
1097 ~~addition~~, the high velocity of the flow and the gradient between ~~steep~~ proximal and
1098 ~~distal~~ zones ~~and more flat toes~~ induce high stress to the flow, resulting in the
1099 formation of distinct surface ridges and troughs with largely variable wavelength
1100 spacing, up to several times larger than the mean lava flow thickness. ~~Furthermore,~~
1101 ~~the rough surface with small blocks and the low volume fraction of microlites of this~~
1102 ~~type of lavas suggest rapid magma extrusion and emplacement (Cashman and~~
1103 ~~Blundy, 2000; Watts et al., 2002).~~

1104 d) Breakout lavas range from thin to thick flows and have the most complex shapes
1105 (high P_k values) with lateral and frontal breakouts, poorly developed levees and fronts
1106 with increasing width and thickness. Thin lavas are cooling-limited with relatively
1107 low viscosities, with lobes and overflows occurring along the flow margins and at the
1108 flow front in areas of low slopes. On the other hand, thicker flows have higher crystal
1109 contents and viscosities, while breakouts are less developed and only occur as simple
1110 structures, mainly in thermally preferential pathways such as the flow margins. ~~Some~~
1111 ~~of these thick flows can be transitional to ridged flows.~~

1112 e) Transitional lavas are common between the different types and exhibit intermediate
1113 features, folding patterns, and shapes between the different types, making difficult
1114 the univocal attribution to a given lava type.



1115

1116 **Figure 17.** Schematic summary of the main types of lava flows identified in the CVZ. x = average
1117 values, * = vent location.

1118 The strength of the proposed morphology-based characterization, mainly based on data
1119 derived from remote observations, **and-classification** is its ready applicability to the analysis
1120 of both terrestrial and extra-terrestrial lava flows. The analysis also provides key parameters
1121 for understanding the main processes which control effusion and emplacement dynamics of
1122 intermediate to silicic, crystal-rich lavas, so complementing existing lava flow classification,
1123 mainly based on the surface morphology characteristics of basaltic lavas.

1124 **Acknowledgments**

1125 This work was supported by the supported by the Agencia Nacional de Investigación y
1126 Desarrollo (ANID) - Becas Chile [72200406, 2019]. The TanDEM-X DEMs were provided
1127 by the German Aerospace Center (DLR) through proposals DEM_GEOL1342 and

1128 DEM_GEOL2956. Alvaro Aravena was financed by the French government IDEX-ISITE
1129 initiative 16-IDEX-0001 (CAP 20-25).

1130 **Author statement**

1131 **Jose Pablo Sepulveda:** Conceptualization, Investigation, Writing - Original draft, Writing -
1132 review & editing, Visualization. **Raffaello Cioni:** Conceptualization, Supervision, Writing -
1133 review & editing, Visualization. **Alvaro Aravena:** Conceptualization, Methodology,
1134 Software, Writing - review & editing, Visualization.

1135 **7. References**

1136 Anderson, S.W., Fink, J.H., 1992. Crease structures: Indicators of emplacement rates and surface
1137 stress regimes of lava flows. *Geol. Soc. Am. Bull.*, 104, 615-625.

1138 Andrews, G.D.M., Kenderes, S.M., Whittington, A.G., Isoma, S.L., Brown, S.R., Pettus, H.D.,
1139 Cole, B.G., Gokey, K.J., 2020. The fold illusion: The origins and implications of ogives on silicic
1140 lavas. *Earth Planet. Sci. Lett.*, 553, 116643. <https://doi.org/10.1016/j.epsl.2020.116643>.

1141 Bertin, D., Amigo, A., 2019. Geología del volcán San Pedro, Región de Antofagasta. Servicio
1142 Nacional de Geología y Minería, Carta Geológica de Chile, Serie Geología Básica. escala 1-50,
1143 000.

1144 Bertin, D., Lara, L., Basualto, D., Amigo, A., Cardona, C., Franco, L., Gil, F., Lazo, J., 2015.
1145 High effusion rates of the Cordon Caulle 2011–2012 eruption (Southern Andes) and their relation
1146 with the quasi-harmonic tremor, *Geophys. Res. Lett.*, 42, 7054–7063,
1147 doi:10.1002/2015GL064624.

1148 Biot, M.A., 1961. Theory of folding of stratified viscoelastic media and its implications in
1149 tectonics and orogenesis. *Geol. Soc. Am. Bull.*, 72(11), 1595-1620.

1150 Blake, S., 1990. Viscoplastic models of lava domes. In: Fink, J.H. (Ed.), *Lava Flows and Domes:
1151 Emplacement Mechanisms and Hazard Implications*. IAVCEI Proc. in *Volcanology*, vol. 2,
1152 Springer, New York, pp. 88-128.

1153 Borgia, A., Linneman, S.R., Spencer, D., Morales, L.D., Brenes, J.A. 1983. Dynamics of lava
1154 flow fronts, Arenal Volcano, Costa Rica. *J. Volcanol. Geotherm. Res.*, 19, 303-329.

1155 Borgia, A., Linneman, S.R., 1990. On the Mechanisms of Lava Flow Emplacement and Volcano
1156 Growth: Arenal, Costa Rica. In: Fink, J.H. (Ed.), *Lava Flows and Domes: Emplacement
1157 Mechanisms and Hazard Implications*. IAVCEI Proc. in *Volcanology*, vol. 2, Springer, New
1158 York, pp. 208-243.

1159 Bottinga, Y., Weill, D., 1972. The viscosity of magmatic silicate liquids: a model for calculation.
1160 *Am. J. Sci.* 272, 438-475.

1161 Bullock, L.A., Gertisser, R., O'Driscoll, B., 2018. Emplacement of the Rocche Rosse rhyolite
1162 lava flow (Lipari, Aeolian Islands). *Bull. Volcanol.*, 80(48) <https://doi.org/10.1007/s00445-018->
1163 1222-4

1164 Calvari, S., Pinkerton, H., 1998. Formation of lava tubes and extensive flow field during the
1165 1991–93 eruption of Mount Etna. *J Geophys Res*, 103, 27291-27302

1166 Caricchi, L., Burlini, L., Ulmer, P., Gerya, T., Vassalli, M., Papale, P., 2007. Non-Newtonian
1167 rheology of crystal-bearing magmas and implications for magma ascent dynamics. *Earth Planet.*
1168 *Sci. Lett.*, 264(3-4), 402-419. <https://doi.org/10.1016/j.epsl.2007.09.032>

1169 Cas, R.A.F., Wright, J.V., 1987. *Volcanic Successions: Modern and Ancient*. Allen and Unwin,
1170 London. 528 p. <http://dx.doi.org/10.1007/978-94-009-3167-1>

1171 Cascante, M., 2015. Evolución geológica y magmática del volcán Isluga, 19° S. Región de
1172 Tarapacá, Chile. Master's Thesis, Universidad de Chile, Santiago, Chile.

1173 Cashman, K., Blundy, J., 2000. Degassing and crystallization of ascending andesite and dacite.
1174 *Philosophical Transactions of The Royal Society*, 358, 1487-1513.

1175 Cashman, K., Soule, S., Mackey, B., Deligne, N., Deardorff, N., Dietterich, H., 2013. How lava
1176 flows: new insights from applications of lidar technologies to lava flow studies. *Geosphere* 9(6),
1177 1664-1680.

1178 Castro, J., Cashman, K.V., 1999. Constraints on rheology of obsidian lavas based on mesoscopic
1179 folds. *J. Struct. Geol.*, 21(7), 807-819.

1180 Castro, J., Cashman, K., Joslin, N., Olmsted, B., 2002. Structural origin of large gas cavities in
1181 the Big Obsidian Flow, Newberry Volcano. *J. Volcanol. Geotherm. Res.*, 114(3-4), 313-330.
1182 [doi.org/10.1016/S0377-0273\(01\)00296-7](https://doi.org/10.1016/S0377-0273(01)00296-7)

1183 Castro, J.M., Schipper, C.I., Mueller, S. P., Militzer, A.S., Amigo, A., Silva Parejas, C., Jacob.,
1184 D., 2013. Storage and eruption of near-liquidus rhyolite magma at Cordón Caulle, Chile. *Bull.*
1185 *Volcanol.*, 75, 702. doi: 10.1007/s00445-013-0702-9

1186 Castruccio, A., Rust, A.C., Sparks, R.S.J., 2010. Rheology and flow of crystal-bearing lavas:
1187 Insights from analogue gravity currents. *Earth Planet. Sci. Lett.*, 297, 471-480.
1188 <https://doi.org/10.1016/j.epsl.2010.06.051>

1189 Castruccio, A., Rust, A. C., Sparks, R.S.J., 2013. Evolution of crust- and core-dominated lava
1190 flows using scaling analysis. *Bull. Volcanol.*, 75 (68). doi: 10.1007/s00445-012-0681-2

1191 Chevrel, M.O., Platz, T., Hauber, E., Baratoux, D., Lavallée, Y., Dingwell, D.B., 2013. Lava flow
1192 rheology: a comparison of morphological and petrological methods. *Earth Planet. Sci. Lett.*, 384,
1193 102-120.

1194 Cioni, R., Funedda, A., 2005. Structural geology of crystal-rich, silicic flows: a case study from
1195 San Pietro Island (Sardinia, Italy). *Geol. Soc. Am.*, 396, 1-14. doi: 10.1130/2005.2396(01).

1196 Cimorelli, C., Costa, A., Mueller, S.P., Mader, H.M., 2011. Rheology of magmas with bimodal
1197 crystal size and shape distributions: Insights from analog experiments. *Geochemistry,*
1198 *Geophysics, Geosystems*, 12, Q07024. doi.org/10.1029/2011GC003606

1199 Costa, A., 2005. Viscosity of high crystal content melts: Dependence on solid fraction. *Geophys.*
1200 *Res. Lett.*, 32, L22308. https://doi.org/10.1029/2005gl024303

1201 Costa, A., Caricchi, L., Bagdassarov, N., 2009. A model for the rheology of particle-bearing
1202 suspensions and partially molten rocks. *Geochemistry, Geophysics, Geosystems*, 10, Q03010.
1203 doi.org/10.1029/2008gc002138

1204 Deardorff, N. D., Cashman, K. V., 2012. Emplacement conditions of the c. 1,600-year bp Collier
1205 Cone lava flow, Oregon: a LiDAR investigation. *Bulletin of Volcanology*, 74,(9), 2051-2066.
1206 Doi: 10.1007/s00445-012-0650-9

1207 Deardorff, N., Booth, A., Cashman, K., 2019. Remote characterization of dominant wavelengths
1208 from surface folding on lava flows using lidar and discrete Fourier transform analyses.
1209 *Geochemistry, Geophysics, Geosystems*, 20, 3952-3970. doi.org/10.1029/2019GC008497

1210 De Reu, J., Bourgeois, J., Bats, M., Zwertvaegher, A., Gelorini, V., De Smedt, P., Chu, W.,
1211 Antrop, M., De Maeyer, P., Finke, P., Van Meirvenne, M., Verniers, J., Crombé, P., 2013.
1212 Application of the topographic position index to heterogeneous landscapes. *Geomorphology*,
1213 186, 39-49. http://dx.doi.org/10.1016/j.geomorph.2012.12.015

1214 Deruelle, B., 1982. Sairecabur volcano, a Plio-Quaternary calc-alkaline massif of the Andes of
1215 Atacama: Petrology. In: III Congreso Geológico Chileno, Concepcion, Chile.

1216 De Silva, S.L., Self, S., Francis, P.W., Drake, R.E., Ramirez, C., 1994. Effusive silicic volcanism
1217 in the Central Andes: The Chao dacite and other young lavas of the Altiplano-Puna Volcanic
1218 Complex. *J. Geophys. Res.*, 99, B9, 17805-17820

1219 De Silva, S.L., Davidson, J.P., Croudace, I.W., Escobar, A., 1993. Volcanological and
1220 petrological evolution of Volcan Tata Sabaya, SW Bolivia. *J. Volcanol. Geotherm. Res.*, 55, pp.
1221 305-335

1222 Dietterich, H. R., Poland, M. P., Schmidt, D. A., Cashman, K. V., Sherrod, D. R., Espinosa, A.
1223 T., 2012. Tracking lava flow emplacement on the east rift zone of Kilauea, Hawaii, with synthetic
1224 aperture radar coherence. *Geochem. Geophys. Geosyst.* 13:Q05001. doi:
1225 10.1029/2011GC004016

1226 Dietterich, H.R., Cashman, K.V., 2014. Channel networks within lava flows: Formation,
1227 evolution, and implications for flow behavior, *J. Geophys. Res. Earth Surf.*, 119, 1704–1724,
1228 doi:10.1002/2014JF003103.

1229 Dietterich, H. R., Cashman, K.V., Rust, C.A., Lev, E., 2015. Diverting lava flows in the lab,
1230 *Nature Geoscience*, 8, 494-496, doi:10.1038/ngeo2470.

- 1231 Dinas, S., Bañon, J.M. 2014. A review on Delaunay Triangulation with application on computer
1232 vision. *International Journal of Computer Science and Engineering*, 3, 2.
- 1233 Dunai, T.J., González López, G.A., Juez-Larré, J., 2005. Oligocene–Miocene age of aridity in the
1234 Atacama Desert revealed by exposure age dating of erosion-sensitive landforms. *Geology*, 33,
1235 321-324
- 1236 Farquharson, J.I., James, M.R., Tuffen, H., 2015. Examining rhyolite lava flow dynamics through
1237 photo-based 3D reconstructions of the 2011–2012 lava flow field at Cordón-Caulle, Chile. *J.*
1238 *Volcanol. Geotherm. Res.*, 304, 336-348.
- 1239 Farrell, J., Karson, J., Soldati, A., Wysocki, R., 2018. Multiple-generation folding and non-coaxial
1240 strain of lava crusts. *Bull. Volcanol.*, 80(84). <https://doi.org/10.1007/s00445-018-1258-5>
- 1241 Farris, R.J., 1968. Prediction of the viscosity of multimodal suspensions from unimodal viscosity
1242 data. *Trans. Soc. Rheol.* 12, 281–301
- 1243 Favalli, M., Fornaciai, A., Nannipieri, L., Harris, A., Calvari, S., Lormand, C., 2018. *Bull.*
1244 *Volcanol.*, 80(29). <https://doi.org/10.1007/s00445-018-1192-6>.
- 1245 Feeley, T.C, Davidson, J.P., Armendia, A., 1993. The volcanic and magmatic evolution of volcan
1246 Ollagüe, a high-K, late Quaternary stratovolcano in the Andean Central Volcanic Zone. *J.*
1247 *Volcanol. Geotherm. Res.*, 54, pp. 221-245
- 1248 Figueroa, O., Deruelle, B., Demaiffe, D., 2009. Genesis of adakite-like lavas of Licancabur
1249 volcano (Chile-Bolivia, central Andes). *C.R. Geoscience* 341, 310–318.
- 1250 Fink, J.H., 1980. Surface folding and viscosity of rhyolite flows. *Geology*, 8(5), 250-254.
- 1251 Fink, J.H., 1983. Structure and emplacement of a rhyolitic obsidian flow: little glass mountain,
1252 medicine lake highland, northern California. *Geol. Soc. Am. Bull.*, 94, 362-380.
- 1253 Fink, J. H., Fletcher, R. C., 1978. Ropy pahoehoe: Surface folding of a viscous fluid. *J. Volcanol.*
1254 *Geotherm. Res.*, 4(1-2), 151-170.
- 1255 Fink, J.H., Griffiths, R.W., 1990. Radial spreading of viscous-gravity currents with solidifying
1256 crust *J. Fluid. Mech.*, 2(21), 485-510.
- 1257 Fink, J.H., Griffiths, R.W., 1998. Morphology, eruption rates, and rheology of lava domes:
1258 insights from laboratory models. *J. Geophys. Res.* 103, 527-545.
- 1259 Gardeweg, M., Cornejo, P., Davidson, J., 1984. Geología del volcan Llullaillaco, altiplano de
1260 Antofagasta, Chile (Andes Centrales). *Rev. Geol. Chile*, 23, pp. 21-37.
- 1261 Gardeweg, M., Amigo, A., Matthews, S.J., Sparks, R.S.J., Clavero, J., 2011. Geología del volcan
1262 Lascar region de Antofagasta. Servicio Nacional de Geología y Minería, Carta Geologica de
1263 Chile. Serie Geología Basica, 131. Escala 1:50,000

1264 Giordano, D., Russell, J.K., Dingwell, D.B., 2008. Viscosity of magmatic liquids: A model. Earth
1265 Planet. Sci. Lett., 271(1-4), 123-134. <https://doi.org/10.1016/j.epsl.2008.03.038>

1266 Giordano, D., 2019. Advances in the rheology of natural multiphase silicate melts: importance
1267 for magma transport and lava flow emplacement. *Ann. Geophys.*, 62, 2, VO216. doi: 10.4401/ag-
1268 7859

1269 Glasbey, C.A., Horgan, C.W., 1995. Image analysis for the Biological Sciences. John Wiley &
1270 Sons, Inc., 605, New York, 218 pp.

1271 Glaze, L., Baloga, S.M., Garry, W.B., Fagents, S.A., Parcheta, C., 2009. A hybrid model for
1272 leveed lava flows: Implications for eruption styles on Mars, *J. Geophys. Res.*, 114, E07001,
1273 doi:10.1029/2008JE0032

1274 Gregg, T.K.P., Fink, J.H., 1995. Quantification of submarine lava-flow morphology through
1275 analog experiments. *Geology*, 23, 73-76.

1276 Gregg, T.K.P., Fink, J.H., 1996. Quantification of extraterrestrial lava flow effusion rates through
1277 laboratory simulations. *J. Geophys. Res.*, 101, 16891-16900.

1278 Gregg, T.K., Fink, J.H., Griffiths, R.W., 1998. Formation of multiple fold generations on lava
1279 flow surfaces: Influence of strain rate, cooling rate, and lava composition. *J. Volcanol. Geotherm.*
1280 *Res.*, 80(3-4), 281-292. [https://doi.org/10.1016/S0377-0273\(97\)00048-6](https://doi.org/10.1016/S0377-0273(97)00048-6)

1281 Gregg, T.K.P., Fink, J.H., 2000. A laboratory investigation into the effects of slope on lava flow
1282 morphology, *J. Volcanol. Geotherm. Res.*, 96, 145-159, doi:10.1016/S0377-0273(99)00148-1.

1283 Griffiths, R.W., Fink, J.H., 1992a. Solidification and morphology of submarine lavas: a
1284 dependence on extrusion rate. *J. Geophys. Res.*, 97, 19729-19737.

1285 Griffiths, R.W., Fink, J.H., 1992b. The morphology of lava flows in planetary environments:
1286 predictions from analog experiments. *J. Geophys. Res.*, 97, 19739-19748.

1287 Griffiths, R.W., Fink, J.H., 1997. Solidifying Bingham extrusions: A model for the growth of
1288 silicic lava domes, *J. Fluid Mech.*, 347, 13-36.

1289 Griffiths, R., 2000. The dynamics of lava flows. *Annu. Rev. Fluid Mech.*, 32(1), 477-518.
1290 <https://doi.org/10.1146/annurev.fluid.32.1.477>

1291 Griffiths, R.W., Kerr, R.C., Cashman, K.V., 2003. Patterns of solidification in channel flows with
1292 surface cooling, *J. Fluid Mech.*, 496, 33-62.

1293 Grosse, P., Orihashi, Y., Guzman, S., Sumino, H., Nagao, K., 2018. Eruptive history of Incahuasi,
1294 Falso Azufre and El Cónдор Quaternary composite volcanoes, southern Central Andes. *Bull.*
1295 *Volcanol.*, 80(44). 10.1007/s00445-018-1221-5

1296 Gualda G.A.R., Ghiorso M.S., Lemons R.V., Carley T.L., 2012. Rhyolite-MELTS: A modified
1297 calibration of MELTS optimized for silica-rich, fluid-bearing magmatic systems. *Journal of*
1298 *Petrology*, 53, 875-890.

- 1299 Hallworth, M.A., Huppert, H.E., Sparks, R.S.J., 1987. A laboratory simulation of basaltic lava
1300 flows. *Mod. Geol.*, 11, 93-107
- 1301 Harris, A.J.L., Flynn, L.P., Matias, O., Rose, W.I., 2002. The thermal stealth flows of Santiaguito
1302 dome, Guatemala: Implications for the cooling and emplacement of dacitic block-lava flows.
1303 *Geol. Soc. Am. Bull.*, 114(5), 533-546. DOI: 10.1130/0016-
1304 7606(2002)114<0533:TTSFOS>2.0.CO;2
- 1305 Harris, A.J.L., Dehn, J., Calvari, S., 2007. Lava effusion rate definition and measurement: a
1306 review. *Bull. Volcanol.*, 70,1-22. doi:10.1007/s00445-007-0120-y
- 1307 Harris, A. J. L., Rowland, S.K., 2009. Effusion rate controls on lava flow length and the role of
1308 heat loss: A review. In: Thordarson, T., Self, S., Larsen, G., Rowland, S.K., Hoskuldsson, A.
1309 (Eds.), *Studies in Volcanology: The Legacy of George Walker*. Special Publications of IAVCEI,
1310 2 , 33-51.
- 1311 Harris, A.J.L., Rowland, S.K., 2015. Lava flows and rheology. In: Sigurdsson, H., Houghton, B.,
1312 McNutt, S.R., Rymer, H., Styx, J., (Eds.), *Encyclopedia of Volcanoes*, 2nd Edition. Academic
1313 Press, 321-342. <https://doi.org/10.1016/C2015-0-00175-7>
- 1314 Harris, A.J.L., Rowland, S., Villeneuve, N., Thordarson, T., 2016. Pāhoehoe, ‘a’ā, and block lava:
1315 an illustrated history of the nomenclature. *Bull. Volcanol.*, 79(7). Doi: 10.1007/s00445-016-
1316 1075-7
- 1317 Harris, A., Mannini, S., Thivet, S., Chevrel, M.O., Gurioli, L., Villeneuve, N., Di Muro, A.,
1318 Peltier, A., 2019. How shear helps lava to flow. *Geology*, 48. <https://doi.org/10.1130/G47110.1>
- 1319 Heckbert, P., 1982. Color image quantization for frame buffer display. *Computer Graphics*, 16,
1320 3, 297-307
- 1321 Hickson, C., Spurgeon, T., Tilling, R., Adam, P., 2013. Factors influencing volcanic hazards and
1322 the morphology of volcanic landforms. In: Shroder, J., James, L., Harden, C., Clague, J. (Eds.),
1323 *Treatise on Geomorphology*, vol. 13. Academic Press, San Diego, CA., pp. 219-242.
1324 <http://dx.doi.org/10.1016/B978-0-12-374739-6.00360-2>
- 1325 Hulme, G., 1974. The interpretation of lava flow morphology. *Geophys.*, 39(2), 361-383.
1326 <https://doi.org/10.1111/j.1365-246X.1974.tb05460.x>
- 1327 Hunt, J. A., Pyle, D. M., Mather, T. A., 2019. The geomorphology, structure, and lava flow
1328 dynamics of peralkaline rift volcanoes from high-resolution digital elevation models.
1329 *Geochemistry, Geophysics, Geosystems*, 20, 1508-1538. <https://doi.org/10.1029/2018GC008085>
- 1330 Jeffreys, H., 1925. The flow of water in an inclined channel of rectangular section. *Philos. Mag.*
1331 *Ser. 6*,49 (293), 793-807.
- 1332 Kereszturi, G. Németh, K., Moufti, M.R., Cappello, A., Murcia, H., Ganci, G., Del Negro, C.,
1333 Procter, J., Zahran, H.M.A., 2016. Emplacement conditions of the 1256AD Al-Madinah lava flow

1334 field in Harrat Rahat, Kingdom of Saudi Arabia-Insights from surface morphology and lava flow
1335 simulations. *J. Volcanol. Geotherm. Res.*, 309, 14-30.

1336 Kerr, R. C., Griffiths, R.W., Cashman, K., 2006. Formation of channelized lava flows on an
1337 unconfined slope, *J. Geophys. Res.*, 111(B10), B10,206, doi:10.1029/2005JB004225.

1338 Kilburn, C., 1990. Surfaces of aa flow-fields on Mount-Etna, Sicily: morphology, rheology,
1339 crystallization and scaling phenomena. In: Fink, J.H. (Ed.), *Lava flows and domes*, IAVCEI
1340 *Proceedings in Volcanology* vol. 2, Springer, New York, pp. 129-156.

1341 Kilburn, R.C., 2004. Fracturing as a quantitative indicator of lava flow dynamics. *J. Volcanol.*
1342 *Geotherm. Res.*, 132, 2-3, 209-224

1343 Klein, J., Mueller, S.P., Castro, J.M., 2017. The influence of crystal size distributions on the
1344 rheology of magmas: New insights from analog experiments. *Geochemistry, Geophysics,*
1345 *Geosystems*, 18, 4055-4073. <https://doi.org/10.1002/2017GC007114>

1346 Klein, J., Mueller, S.P., Helo, C., Schweitzer, S., Gurioli, L. Castro, J.M., 2018. An expanded
1347 model and application of the combined effect of crystal-size distribution and crystal shape on the
1348 relative viscosity of magmas. *J. Volcanol. Geotherm. Res.*, S0377-0273(17)30725-4. doi:
1349 doi:10.1016/j.jvolgeores.2018.04.018

1350 Krieger, G., Moreira, A., Fiedler, H., Hajnsek, I., Werner, M., Younis, M., Zink, M., 2007.
1351 TanDEM-X: A satellite formation for high-resolution SAR interferometry. *IEEE Transactions on*
1352 *Geoscience and Remote Sensing*, 45(11), 3317–3341.

1353 Krieger, I.M., Dougherty, T.J., 1959. A mechanism for non-Newtonian flow in suspensions of
1354 rigid spheres. *J. Rheol.* 3, 137.

1355 Latutrie, B., Harris, A., Médard, E., Gurioli, L., 2017. Eruption and emplacement dynamics of a
1356 thick trachytic lava flow of the Sancy Volcano (France). *Bull. Volcanol.*, 79(4).
1357 doi:10.1007/s00445-016-1084-6

1358 Leggett, T.N., Befus, K.S., Kenderes, S.M., 2020. Rhyolite lava emplacement dynamics inferred
1359 from surface morphology. *J. Volcanol. Geotherm. Res.*, 395, 106850
1360 <https://doi.org/10.1016/j.jvolgeores.2020.106850>

1361 Lescinsky, D.T., Skoblenick, S.V., Mansinha, L., 2007. Automated identification of lava flow
1362 structures using local Fourier spectrum of digital elevation data. *J. Geophys. Res.*, 112(B05212).
1363 doi:10.1029/2006 JB004263

1364 Lev, E., Rumpf, E., Dietterich, H., 2019. Analog experiments of lava flow emplacement. *Ann.*
1365 *Geophys.*, 62, 2 (vo225). doi: 10.4401/ag-7843

1366 Lister, J. R., 1992. Viscous flows down an inclined plane from point and line sources. *J. Fluid*
1367 *Mech.*, 242, 631–653.

- 1368 Lyman, A.W., Koenig, E., Fink, J., 2004. Predicting yield strengths and effusion rates of lava
1369 domes from morphology and underlying topography. *J. Volcanol. Geotherm. Res.*, 129, 125-138.
1370 doi:10.1016/S0377-0273(03)00236-1
- 1371 Macdonald, G.A., 1953. Pahoehoe, aa and block lava. *Am. J. Sci.*, 251. pp. 169-191.
- 1372 Macdonald, G.A., 1967. Forms and structures of extrusive basaltic rocks. In: Hess H.H.,
1373 Poldervaart, A. (Eds-), *The Poldervaart Treatise on rocks of basaltic composition*. Interscience,
1374 New York, 1-61.
- 1375 Macdonald, G.A., 1972. *Volcanoes*. Prentice Hall Inc., Englewood Cliffs, 501 pp.
- 1376 Magnall, N., James, M.R., Tuffen, H., Vye-Brown, C., 2017. Emplacing a Cooling-Limited
1377 Rhyolite Lava Flow: Similarities with Basaltic Lava Flows. *Front. Earth Sci.*, 5(44) doi.org /10
1378 .3389/feart.2017.00044
- 1379 Magnall, N., James, M.R., Tuffen, H., Vye-Brown, C., Schipper, C.I., Castro, J., Gerard Davies,
1380 A., 2018. The origin and evolution of breakouts in a cooling-limited rhyolite lava flow. *Geol.*
1381 *Soc. Am. Bull.*, 131(1/2), 137–154. doi.org /10 .1130 /B31931.1
- 1382 Mamani, M, Wörner, G., Sempere, T., 2010. Geochemical variations in igneous rocks of the
1383 Central Andean orocline (13°S to 18°S): Tracing crustal thickening and magma generation
1384 through time and space. *Geol. Soc. Am. Bull.*, 122(1/2), pp. 162-182. doi: 10.1130/B26538.1
- 1385 Manley, C.R., Fink, J.H., 1987. Internal textures of rhyolite flows as revealed by research drilling.
1386 *Geology*, 15, 549-552. doi: 10.1130/0091-7613(1987)15<549:ITORFA>2.0.CO;2
- 1387 Martinez, S., 2019. Evolución magmática y geoquímica de la cadena volcánica Olca-Paruma
1388 (20°57'S-68°30'O), norte de Chile. Undergraduated Thesis, Universidad Católica del Norte,
1389 Antofagasta, Chile.
- 1390 Mueller, S.P., Llewellyn, E.W., Mader, H.M., 2011. The effect of particle shape on suspension
1391 viscosity and implications for magmatic flows. *Geophys. Res. Lett.*, 38, L13316.
1392 doi.org/10.1029/2011GL047167
- 1393 Naranjo, J.A., 1992. Chemistry and petrological evolution of the Lastarria volcanic complex in
1394 the north Chilean Andes. *Geol. Mag.*, 129(6), pp. 723-740.
- 1395 Naranjo, J., Sparks, R., Stasiuk, M., Moreno, H., Ablay, G., 1992. Morphological, structural and
1396 textural variations in the 1988–1990 andesite lava of Lonquimay Volcano, Chile. *Geol. Mag.*,
1397 129(6), 657–678. doi.org/10.1017/S0016756800008426
- 1398 Naranjo, J., Villa, V., Venegas, C., 2013. Geología de las áreas Salar de Pajonales y Cerro Moño,
1399 regiones de Antofagasta y Atacama. Servicio Nacional de Geología y Minería, Carta Geológica
1400 de Chile, Serie Geología Básica, 153-154.

- 1401 Navarro-Ochoa, C., Gavilanes-Ruiz, J.C., Cortes-Cortes, A., 2002. Movement and emplacement
1402 of lava flows at Volcan de Colima, Mexico: November 1998-February 1999. *J. Volcanol.*
1403 *Geotherm. Res.*, 117, 155-167.
- 1404 Pallister, J.S., Diefenbach, A.K., Burton, W.C., Muñoz, J., Griswold, J.P., Lara, L.E. Lowenstern,
1405 J.B., Valenzuela, C.E., 2013. The Chaitén rhyolite lava dome: Eruption sequence, lava dome
1406 volumes, rapid effusion rates and source of the rhyolite magma. *Andean Geology*, 40(2).
1407 doi.org/10.5027/andgeoV40n2-a06
- 1408 Persoon, E., Fu, K.S., 1977. Shape Discrimination Using Fourier Descriptors. *IEEE Transactions*
1409 *on Systems, Man, and Cybernetics*, 7(3), pp. 170-179.
- 1410 Pinkerton, H., Sparks, R.S.J., 1976. The 1975 sub-terminal lavas, Mount Etna: a case history of
1411 the formation of a compound lava field. *J. Volcanol. Geotherm. Res.*, 1, 167-182.
- 1412 Pinkerton, H., Stevenson, R.J., 1992. Methods of determining the rheological properties of
1413 magmas at sub-liquidus temperatures. *J. Volcanol. Geotherm. Res.*, 53, 47-66.
- 1414 Pinkerton, H., Wilson, L., 1994. Factors controlling the lengths of channel-fed lava flows. *Bull.*
1415 *Volcanol.*, 56, 108-120
- 1416 Pyle, D.M., Elliott, J.R., 2006. Quantitative morphology, recent evolution, and future activity of
1417 the Kameni Islands volcano, Santorini, Greece. *Geosphere*, 2(5), 253–268
- 1418 Reyes Hardy, M.P., Aguilera Barraza, F., Sepulveda Birke, JP., Esquivel Cáceres, A., Inostroza
1419 Pizarro, M. 2021. GIS-based volcanic hazards, vulnerability and risks assessment of the Guallatiri
1420 Volcano, Arica y Parinacota Region, Chile. *J. S. Am. Earth. Sci.*, 109, 103262.
- 1421 Richardson, P, Karlstrom, L., 2019. The multi-scale influence of topography on lava flow
1422 morphology. *Bull. Volcanol.*, 81, 21. <https://doi.org/10.1007/s00445-019-1278-9>
- 1423 Rivera, M., Martin, H., Le Penneç, H.L., Thouret, J.C., Gourgad, A., Gerbe, M.C., 2017. Petro-
1424 geochemical constraints on the source and evolution of magmas at El Misti volcano (Peru).
1425 *Lithos*, 268-271, pp. 240-259. doi.org/10.1016/j.lithos.2016.11.009
- 1426 Rodriguez, I., Roche, O., Moune, S., Aguilera, F., Campos, E., Pizarro, M., 2015. Evolution of
1427 Iruputuncu volcano, Central Andes, northern Chile. *J. S. Am. Earth Sci.*, 63, pp. 385-399.
1428 <http://dx.doi.org/10.1016/j.jsames.2015.08.012>
- 1429 Sato, H., Suzuki-Kamata, k., Sato, E., Sano, K., Wada, K., Imura, R., 2013. Viscosity of andesitic
1430 lava and its implications for possible drain-back processes in the 2011 eruption of the
1431 Shinmoedake volcano, Japan. *Earth Planets Space*, 65, 623–631.
- 1432 Schneider, C.A., Rasband, W.S., Eliceiri, K.W., 2012. NIH Image to ImageJ: 25 years of image
1433 analysis. *Nature Methods*, 9(7), 671–675. doi:10.1038/nmeth.2089

- 1434 Selles, D., Gardeweg, M., 2018. Geología del área Ascotán-Cerro Inacaliri, Región de
1435 Antofagasta. Servicio Nacional de Geología y Minería, Carta Geológica de Chile. Serie Geología
1436 Básica, 190. Escala 1:50,000. doi: 10.13140/RG.2.2.30946.84165
- 1437 Sepulveda, J.P., Aguilera, F., Inostroza, M., Reyes, M.P., 2021. Geological evolution of the
1438 Guallatiri volcano, Arica y Parinacota Region, northern Chile. *J. S. Am. Earth Sci.*, 107(103117).
1439 <https://doi.org/10.1016/j.jsames.2020.103117>
- 1440 Shaw, H.R., 1972. Viscosities of magmatic silicate liquids: An empirical method of prediction.
1441 *Am. J. Sci.* 272, 870-893.
- 1442 Sparks, R.S.J., Folkes, C.B., Humphreys, M.C.S., Barfod, D.N., Clavero, J., Sunagua, M.C.,
1443 McNutt, S.R., Pritchard, M.E., 2008. Uturuncu volcano, Bolivia: volcanic unrest due to mid-
1444 crustal magma intrusion. *Am. J. Sci.*, 308, pp. 727-769, doi: 10.2475/06.2008.01
- 1445 Stern, C., 2004. Active Andean volcanism: Its geologic and tectonic setting. *Rev. Geol. Chile*,
1446 31(2). Doi: 10.4067/S0716-02082004000200001
- 1447 Stockwell, R., Mansinha, L., Lowe, R., 1996. Localization of the complex spectrum: The S-
1448 transform. *IEEE Trans. Signal Process.*, 44(4) 998–1001
- 1449 Stockwell, R., 2007. A basis for efficient representation of the S-transform. *Digital Signal*
1450 *Processing*, 17, 371-393. Doi: 10.1016/j.dsp.2006.04.006
- 1451 Swanson, S. E., Naney, M. T., Westrich, H. R., Eichelberger, J. C., 1989. Crystallization history
1452 of Obsidian dome, Inyo domes, California. *Bulletin of Volcanology*, 51(3), 161-176.
- 1453 Tolometti, G.D., Neish, C.D., Osinski, G.R., Hughes, S.S., Kobs Nawotniak, S.E., 2020.
1454 Interpretations of lava flow properties from radar remote sensing data. *Planet. Space Sci.*, 190,
1455 104991. <https://doi.org/10.1016/j.pss.2020.104991>
- 1456 Tuffen, H., James, M.R., Castro, J.M., Schipper, C.I., 2013. Exceptional mobility of an advancing
1457 rhyolitic obsidian flow at Cordón Caulle volcano in Chile. *Nature Communications*, 4(1).
1458 <https://doi.org/10.1038/ncomms3709>
- 1459 Vallance, J.W., Schneider, D.J., Schilling, S.P., 2008. Growth of the 2004-2006 lava-dome
1460 complex at Mount St. Helens, Washington. *A Volcano Rekindled, 2004-2006*.
- 1461 Wadge, W., Voight, B., Sparks, R.S.J., Cole, P.D., Loughlin, S.C., Robertson, R.E.A., 2014. An
1462 overview of the eruption of Soufriere Hills Volcano, Montserrat from 2000 to 2010. In: Wadge,
1463 G., Robertson, R.E.A., Voight, B. (Eds.), *The Eruption of Soufriere Hills Volcano, Montserrat*
1464 *from 2000 to 2010*. Geological Society, London, *Memoirs*, 39. <http://dx.doi.org/10.1144/M39>.
- 1465 Walker, G. P. L., 1967. Thickness and Viscosity of Etnean Lavas. *Nature*, 213, 484-485.
- 1466 Walker, G.L.P., 1972. Compound and simple lava flows and flood basalts. *Bull. Volcanol.*, 35,
1467 579-590.

- 1468 Walker, G.P.L., 1973. Factors controlling the lengths of lava flows. *Philos. Trans. R. Soc. London*
1469 274, A107–A118
- 1470 Watts, R.B., Herd, R.A., Sparks, R.S.J., Young, S.R., 2002. Growth patterns and emplacement
1471 of the andesitic lava dome at Soufrière Hills Volcano, Montserrat. In: Druitt, T.T., Kokelaar, B.P.
1472 (Eds). *The Eruption of Soufrière Hills Volcano, Montserrat, from 1995 to 1999*. Geological
1473 Society, London, *Memoirs*, 21.
- 1474 Wentworth, C.K., Macdonald, G.A., 1953. Structures and forms of basaltic rocks in Hawaii.
1475 *Bulletin 994, USGS int. Report*, 98 pp.
- 1476 Wörner, G., Lopez-Escobar, L., Moorbath, S., Horn, S., Entenmann, J., Harmon, R.S., Davidson,
1477 J.P., 1992. Variaciones geoquímicas, locales y regionales, en el frente volcánico cuaternario de
1478 los andes centrales (17° 30' -22° 00' S). Norte de Chile. *Rev. Geol. Chile* 19, 37-55.
- 1479 Wörner, G., Schildgen, T.F., Reich, M., 2018. The Central Andes: Elements of an Extreme Land.
1480 *Elements*, 14, pp. 225-23

